

Development of Nickel Hydroxide/Oxide Composite for Application in Next Generation
Electrochemical Capacitors

by

Brian Kihun Kim

A thesis

presented to the University of Waterloo

in fulfillment of the

thesis requirement for the degree of

Master of Applied Science

in

Chemical Engineering

Waterloo, Ontario, Canada, 2014

© Brian Kihun Kim 2014

Author's Declaration

I hereby declare that I am the sole author of this thesis. This is a true copy of my thesis, including any required final revisions, as accepted by my examiners.

I understand that my thesis maybe made electronically available to the public.

Abstract

With the world's increasing energy demand and the depletion of fossil fuels, there is a growing demand for the development of alternative and clean energy sources. Batteries and fuel cell technologies have been cited as next generation technologies to provide sustainable energy; however, these technologies are insufficient in supplying high power in short time periods that can be produced by oil as an energy source. In contrast, electrochemical capacitors possess fast charging/discharging capabilities with high power output. As a result, the use of electrochemical capacitors in commercial applications has generated strong interest. Examples of commercial applications include emergency back-up power, consumer electronics, and hybrid vehicles.

Commercially available electrochemical capacitors are based on carbonaceous materials with high surface area, excellent electrical conductivity, and wettability which statically store the charges in pores. In contrast, pseudocapacitive materials, namely transition metals, utilize fast reversible faradaic reactions on the surface of the materials which allow for greater energy storage than carbonaceous materials. Currently, many research activities are being focused on pseudocapacitive materials in an effort to enhance their energy storage capabilities.

This thesis presents research on a pseudocapacitive material: nickel hydroxide/oxide hybrid. Also, it identifies the hybrid material's lack of conductivity which can negatively impact its

capacitive performance. An addition of carbon supports is recommended to enhance the conductivity.

There are two parts to this study. The first study addresses the synthesis of the nickel hybrid structures through solvothermal process and calcination. The materials are thoroughly analyzed through physical and electrochemical characterizations. The issue of using the hybrid material as pseudocapacitor electrodes are identified at this stage.

The second part of the study addresses the effect of different carbon additives in the nickel hybrid material. Commonly known carbon additives are incorporated into the nickel hybrid material and analyzed through electrochemical characterization to distinguish the best carbon support for the nickel hydroxide/oxide.

Acknowledgements

I would first like to give thanks to my beloved family and friends, especially Emily Minyoung Park, for their endless support throughout my graduate study in the university. A special thank you goes to my supervisor, Dr. Aiping Yu for her academic advice, support, and presenting me with opportunities to participate in other projects, including the ones with other research groups. I would also like to thank Dr. Zhongwei Chen and my colleagues including: Victor Chabot, Gregory Liu, Abdul Rahman, Abel Sy, Hey Woong Park, Fathy Hassan, Dong Un Lee, Drew Higgins, Hadis Zarrin, Ja Yeon Choi, Min Ho Seo, Moon Gyu Park, Ariful Hoque, Jason Wu, and Jordan Scott for their assistance and support.

Table of Contents

Author's Declaration	ii
Abstract.....	iii
Acknowledgements	v
Table of Contents.....	vi
List of Figures.....	viii
List of Tables	xii
List of Abbreviations, Symbols and Nomenclature.....	xiii
Chapter 1: Introduction of Thesis Project.....	1
1.1. Summary of Objectives and Motivation.....	2
1.2 Organization of Thesis.....	3
Chapter 2: Introduction to Electrochemical Capacitors.....	5
2.1 History of Electrochemical Capacitors	5
2.2 Types of Electrochemical Capacitors	6
2.2.1 Conventional Capacitors.....	6
2.2.2 Electrostatic Double-Layer Capacitors (EDLC).....	8
2.2.3 Electrochemical Pseudocapacitors.....	9
2.2.4 Asymmetric Capacitors	10
2.3 Applications.....	11
2.3.1 Consumer Applications	11
2.3.2 Public Sector Application	12
2.3.3 Public Transportation Application.....	12
2.3.4 Future Prospective Application	13
2.4 Challenges and Perspectives.....	15
2.5 Electrodes	16
2.5.1 EDLC Materials.....	16
2.5.2 Pseudocapacitor Materials	20
2.6 Electrolytes	25
2.6.1 Aqueous Electrolytes	26
2.6.2 Organic Electrolytes	27
2.6.3 Ionic Liquids (ILs).....	28
2.7 Separators and Current Collectors	29
2.8 Physical Characterization Techniques	31
2.8.1 X-Ray Diffraction (XRD).....	31
2.8.2 Scanning Electron Microscopy (SEM).....	32
2.8.3 Brunauer-Emmett-Teller (BET) Surface Analysis	32
2.8.4 Four-Point Probe Method	33

2.9	Electrochemical Characterization Techniques.....	34
2.9.1	Electrochemical Cell Design	34
2.9.2	Cyclic Voltammetry (CV)	37
2.9.3	Galvanostatic Charge-Discharge (GCD)	40
2.9.4	Electrochemical Impedance Spectroscopy (EIS).....	41
2.9.5	Energy Density and Power Density	43
2.9.6	Cycle Stability	44
Chapter 3: Nickel Hydroxide/Oxide Hybrid Flower Structure.....		46
3.1	Introduction and Motivation	46
3.2	Experimental Procedures	47
3.2.1	Synthesis of Nickel Hydroxide/Oxide Hybrid.....	47
3.2.2	Physical Characterization	48
3.2.3	Electrochemical Characterization	49
3.3	Results and Discussion	49
3.3.1	XRD Characterization	49
3.3.2	SEM and BET Characterization	51
3.3.3	Electrochemical Analysis	54
3.4	The Effects of Carbon.....	63
3.5	Experimental Procedure.....	64
3.5.1	Synthesis of Reduced Graphene Oxide (rGO).....	64
3.5.2	Preparation of Nickel Hybrid Composite with Carbon Supports	64
3.6	Results and Discussions.....	65
3.7	Summary.....	71
Chapter 4: Perspectives of Future Work.....		73
References		74
Appendix		93

List of Figures

Figure 1: A Ragone plot for significant energy storage and conversion devices.	2
Figure 2: Charged state of conventional capacitors.....	7
Figure 3: An accumulation of ionic charges in the interface formed between electrolyte and electrodes.....	8
Figure 4: Schematic of an asymmetric MnO ₂ -graphene/AC EC [17]. © Wiley.....	11
Figure 5: Concept of integrated energy storage in wearable electronics [28]. © RCS Publications. ..	14
Figure 6: (a) Transmission electron microscope (TEM) image of catalytically grown carbon nanotubes [35]. © AIP Publishing. (b) Scanning electron microscope (SEM) image of carbon nanotube forests [36]. © ACS Publications.....	18
Figure 7: Illustration of 2-D graphene sheet as the building blocks for other carbon materials such as particle, 1-D CNT, and 3-D graphite [41]. © ACS Publications.....	19
Figure 8: (a) Model of graphene sheets separated by CNTs [43]. © ACS Publications. (b) Nitrogen-doped graphene structure [44]. © RSC Publications.....	20
Figure 9: SEM images illustrating the detail morphologies of (a) brush-like Co ₃ O ₄ nanowire [51]. © ACS Publications. (b) MnO ₂ nanowire [52]. © Elsevier. (c) NiO nanopetals [53]. © Elsevier. (d) V ₂ O ₅ nanoporous network [54]. © ACS Publications.	22
Figure 10: Illustration of conducting polymer's charging/discharging mechanism with two doping states: (a) <i>p</i> -doping and (b) <i>n</i> -doping [56]. © Elsevier.....	23
Figure 11: SEM images of (a) PANI arrays on GO sheet [59]. © ACS Publications. (b) PPY deposited on graphene [60]. © ACS Publications.	24
Figure 12: Illustration of energy density of two electrode cell as a function of voltage window and specific capacitance of various electrolytes [62]. © ECS Publications.	26

Figure 13: Illustration of energy density of two electrode cells as a function of voltage window and specific capacitance of various electrolytes [66]. © AAAS Publications.....	29
Figure 14: SEM images of (a) Millipore JVWP separator with fibrous structure and (b) GE Osmotics K50CP01300 separator with monolithic/defined pores [67]. © ECS Publications.	30
Figure 15: Schematic of the four-point probe technique	34
Figure 16: Schematic drawing of three-electrode system: (a) working electrode, (b) reference electrode, and (c) counter electrode [73]. © Elsevier.	35
Figure 17: Illustration of a two-electrode system [74]. © Elsevier.	36
Figure 18: CV curves of (a) ideal capacitor, (b) EDLC, and (c) pseudocapacitive materials.	38
Figure 19: CV curve of ordered graphitic mesoporous carbon at different scan rates [75]. © Elsevier.	39
Figure 20: GCD plots of (a) EDLC and (b) pseudocapacitive material.	40
Figure 21: Schematic representation of the Nyquist plot of (a) an ideal capacitor and (b) an EC [77]. © Elsevier.	42
Figure 22: Performance retention versus cycle number for CNT-sponge and MnO ₂ -CNT-sponge [78]. © ACS Publications.....	45
Figure 23: XRD patterns of NiO-0min, NiO-40min, NiO-2hr, and NiO-4hr [107]. © Elsevier	50
Figure 24: SEM images of (A, B) NiO-0min, (C, D) NiO-40min, (E, F) NiO-2hr, and (G, H) NiO-4hr [107]. © Elsevier	52
Figure 25: (A) Nitrogen adsorption/desorption isotherms of NiO-0min, NiO-40min, NiO-2hr, and NiO-4hr; (B) Pore distribution of NiO-0min, NiO-40min, NiO-2hr, and NiO-4hr [107]. © Elsevier ..	53
Figure 26: Cyclic voltammograms of NiO-0min, NiO-40min, NiO-2hr, and NiO-4hr at (A) 0.005V/s and (B) 0.1V/s; (C) Comparison of scan rate dependent specific capacitance of NiO-0min, NiO-40min, NiO-2hr, and NiO-4hr; and (D) Specific capacitance percentage drop of NiO-0min, NiO-40min, NiO-2hr, and NiO-4hr from scan rate at 0.005 V/s to 0.1 V/s [107]. © Elsevier.....	56

Figure 27: Galvanostatic charge-discharge curve of NiO-0min, NiO-40min, NiO-2hr, and NiO-4hr at (A) 2 A/g and (B) 10 A/g; (C) Comparison of applied current dependent specific capacitance of NiO-0min, NiO-40min, NiO-2hr, and NiO-4hr; and (D) Specific capacitance percentage drop of NiO-0min, NiO-40min, NiO-2hr, and NiO-4hr from applied current at 2 A/g to 10 A/g [107]. © Elsevier.....59

Figure 28: (A) Nyquist impedance spectra of NiO-0min, NiO-40min, NiO-2hr, and NiO-4hr; the inset shows impedance at high frequency region; (B) Equivalent circuit fitted for the impedance spectra where R_{csr} is the electrical series resistance, C_d is the double layer capacitance, R_{it} is the ionic charge transfer resistance, C_{film} is the film capacitance, W is the Warburg diffusion resistance, R_{et} is the electron charge transfer resistance, and C_{ps} is the pseudocapacitance; (C) Electrical conductivity of NiO-0min, NiO-40min, NiO-2hr, and NiO-4hr in logarithmic scale from four-point probe technique [107]. © Elsevier.....61

Figure 29: Cyclic voltammograms of NiO-40min, NiO/KB, NiO/rGO, NiO/MWCNT, and NiO/SWCNT at (A) 0.005 V/s and (B) 0.1 V/s; (C) Comparison of scan rate dependent specific capacitance of NiO-40min, NiO/KB, NiO/rGO, NiO/MWCNT, and NiO/SWCNT; and (D) Specific capacitance percentage drop of NiO-40min, NiO/KB, NiO/rGO, NiO/MWCNT, and NiO/SWCNT from scan rate at 0.005 V/s to 0.1 V/s [107]. © Elsevier.....66

Figure 30: Galvanostatic charge-discharge curve of NiO-40min, NiO/KB, NiO/rGO, NiO/MWCNT, and NiO/SWCNT at (A) 2 A/g and (B) 10 A/g; (C) Comparison of applied current dependent specific capacitance of NiO-40min, NiO/KB, NiO/rGO, NiO/MWCNT, and NiO/SWCNT; and (D) Specific capacitance percentage drop of NiO-40min, NiO/KB, NiO/rGO, NiO/MWCNT, and NiO/SWCNT from applied current at 2 A/g to 10 A/g [107]. © Elsevier.....68

Figure 31: (A) Nyquist impedance spectra of NiO-40min, NiO/KB, NiO/rGO, NiO/MWCNT, and NiO/SWCNT; the inset shows impedance at high frequency region; (B) Equivalent circuit fitted for the impedance spectra where R_{csr} is the electrical series resistance, C_d is the double layer capacitance, R_{it} is the ionic charge transfer resistance, C_{film} is the film capacitance, W is the Warburg diffusion

resistance, R_{et} is the electron charge transfer resistance, and C_{ps} is the pseudocapacitance [107]. ©

Elsevier69

Figure 32: (A) Cycle stability of NiO-40min, NiO/KB, NiO/rGO, NiO/MWCNT, and NiO/SWCNT at a current density of 10 A/g (B) Ragone plot of NiO-40min, NiO/KB, NiO/rGO, NiO/MWCNT, and NiO/SWCNT [107]. © Elsevier70

List of Tables

Table 1: Morphology and performance of currently researched metal oxides for pseudocapacitor applications.....	21
Table 2: Density, ionic resistivity, and voltage window for various electrolytes [61].	25
Table 3: BET surface area and average pore diameter of NiO-0min, NiO-40min, NiO-2hr, and NiO-4hr.....	53
Table 4: Specific capacitance value of NiO-0min, NiO-40min, NiO-2hr, and NiO-4hr at scan rate of 0.005 V/s and 0.1 V/s	55
Table 5: Specific capacitance value of NiO-0min, NiO-40min, NiO-2hr, and NiO-4hr at current density of 2 A/g and 10 A/g.....	59
Table 6: Fitted R_{est} and combination of R_{it} and R_{et} of NiO-0min, NiO-40min, NiO-2hr, and NiO-4hr.	61
Table 7: Specific capacitance value of NiO-40min, NiO/KB, NiO/rGO, NiO/MWCNT, and NiO/SWCNT at current density of 2 A/g and 10 A/g.....	67

List of Abbreviations, Symbols and Nomenclature

A	Contact Area
AC	Activated Carbon
BET	Brunauer-Emmett-Teller
C	Capacitance
C_s	Specific Capacitance
CNT	Carbon Nanotubes
CV	Cyclic Voltammetry
d	Distance
DDI	Double Deionized Water
E.D.	Specific Energy Density
EC	Electrochemical Capacitor
EDLC	Electric Double-Layer Capacitor
EDR	Equivalent Distributed Resistance
EIS	Electrochemical Impedance Spectroscopy
ESR	Equivalent Series Resistance
F	Farad
GCD	Galvanostatic Charge-Discharge
GE	General Electric
GO	Graphene Oxide
I	Current

I_A	Applied Current Density
IL	Ionic Liquid
KB	Ketjenblack
L	Length
LSG	Laser-Scribed Graphene
m	Mass
MWCNT	Multi-walled Carbon Nanotubes
NEC	Nippon Electric Company
NHE	Normal Hydrogen Electrode
PANI	Polyaniline
PC	Polycarbonate
$P.D._{Avg}$	Average Specific Power Density
$P.D._{Max}$	Maximum Specific Power Density
PPY	Polypyrrole
PRI	Pinnacle Research Institute
rGO	Reduced Graphene Oxide
R_{esr}	Equivalent Series Resistance
R_{it}	Ionic Charge Transfer Resistance
R_{et}	Electron Charge Transfer Resistance
SCE	Saturated Calomel Electrode
SDS	Sodium Dodecyl Sulfate
SEM	Scanning Electron Microscopy

SOHIO	Standard Oil of Ohio
SWCNT	Single-walled Carbon Nanotubes
Δt	Total Discharging Time
T	Thickness
ΔV	Voltage Drop, Potential Difference
V_R	Potential Range
V_S	Scan Rate
W	Width
XRD	X-Ray Diffraction
Z' , Z_{re}	Real Resistance
Z'' , Z_{im}	Imaginary Resistance
dV/dt	Slope of Discharging GCD Curve
ε	Permittivity
$\int i dV$	Integrated Area

Chapter 1: Introduction of Thesis Project

The depletion of fossil fuels and the global warming crisis has led the international community to develop alternative and clean energy system. Currently, batteries and fuel cell technologies are being heavily researched to meet this energy demand; however the two technologies lack the high power density which can be supplied by fuel. Extensive operation beyond the limits of batteries can induce side reactions and lower battery efficiency. Over time, this stress will damage the internal structure and reduce the cycle lifetime of batteries.

Electrochemical capacitors (ECs), also known as supercapacitors, possess numerous advantages that complement the many deficiencies of other energy storage devices. Their long cycling lifetime, high power density, and low maintenance cost have aroused great interest academically and commercially, making them more attractive and versatile as high-powered energy storages. They are capable of bridging the gap between batteries/fuel cells with low power densities and energy-lacking capacitors as shown in **Figure 1**.

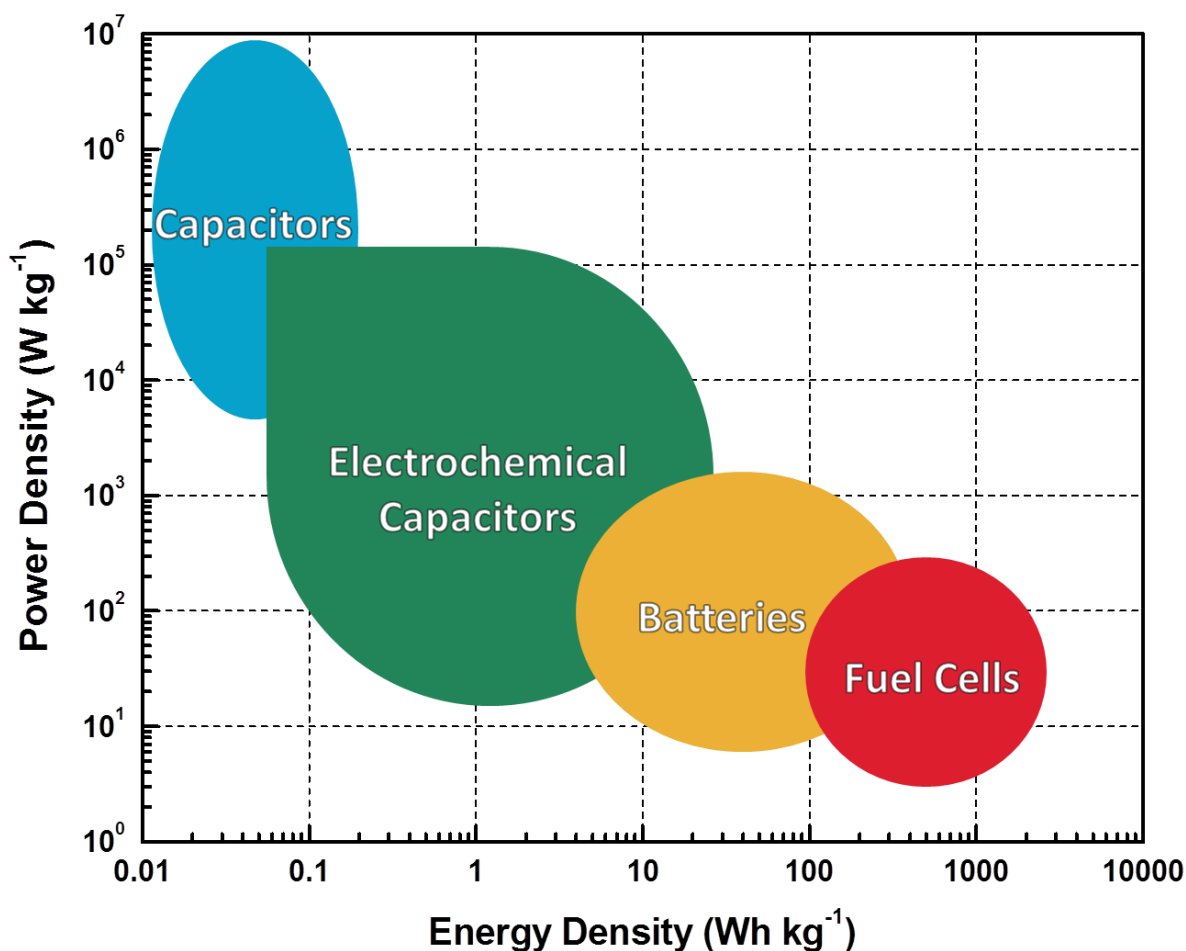


Figure 1: A Ragone plot for significant energy storage and conversion devices.

1.1. Summary of Objectives and Motivation

The project is focused on developing materials for EC electrodes. Materials used in EC electrodes are broadly categorized into carbonaceous materials, pseudocapacitive materials such as transition metals and electrically conductive polymers. For this study, a transition metal oxide, nickel oxide, is selected for its high theoretical capacitance and abundance. Nickel oxide can be produced in many forms and our motivation is to synthesize a high performing nickel oxide.

The first part of this project is to physically and electrochemically analyze synthesized nickel hydroxide/oxide material. The objective of this part is to demonstrate that the nickel hybrid structure outperforms the nickel oxide and nickel hydroxide on its own. Moreover, the study reveals that nickel hybrid structure requires additives to enhance its conductivity which leads to the second part of the project.

The objective of the second part of this study is to evaluate the effects of carbon additives to the nickel hybrid structure. Different types of carbonaceous materials were incorporated into the pseudocapacitive material to improve the conductivity and the composites were electrochemically characterized to verify their capacitive performance.

1.2 Organization of Thesis

The thesis is divided into four chapters. Chapter 1 briefly introduces ECs and discusses the motivations for the project. Chapter 2 provides details on the history of ECs, the different types of ECs, the components of an EC, and the theory behind the characterization and analysis techniques performed in the preparation of this thesis. A literature review on the electrode materials, electrolytes, separators, and current collectors is also provided, along with a discussion of Real-world applications of ECs to inform the readers on the current contribution of ECs in the energy market. Chapter 3 describes the synthesis of nickel hydroxide/oxide material and discusses the effect of carbon additives to the nickel hybrid material. This chapter includes motivations, experimental procedures, characterizations,

results, and they are based on previously published work. Chapter 4 summarizes the project results and suggests possible direction for future work.

Chapter 2: Introduction to Electrochemical Capacitors

2.1 History of Electrochemical Capacitors

Long before the development of capacitors, people discovered that rubbing amber with a cloth induced small particles to attract each other. This unexplained phenomenon was later developed into the very first capacitor called a Leyden jar in 1745. The jar is composed of glass and the interior/exterior surfaces of the jar are laminated with metal foils, acting as conductive plates [1]. After the development of the Leyden jar, the capacitor technology rapidly evolved. In 1957, Howard Becker of General Electric (GE) patented the first EC through pioneering a capacitor with porous carbon electrodes and sulfuric acid electrolytes [2]. In 1970, Standard Oil of Ohio (SOHIO) invented a carbon-based electrolytic capacitor; the technology was licensed to Nippon Electric Company (NEC) who commercialized the first aqueous electrolyte capacitors for back up memory in electronic devices [3, 4]. Numerous companies including Pinnacle Research Institute (PRI) initiated the design and manufacture of ECs with low internal resistances for high-powered portable energy storage [5]. In the late 20th century, Maxwell Technologies inherited PRI's development and produced their own brand of ECs called "Boost Caps". Through continuous development, high-performing ECs are currently manufactured and are available in the market.

2.2 Types of Electrochemical Capacitors

The Leydan Jar was the first capacitor invented and it has since evolved into the conventional capacitor which is used in electric circuit applications to store small amounts of charge. Further research has led to the invention of electric double-layer capacitors (EDLCs) as the first ECs which are capable of accumulating exceptionally high amounts of charge. Growing development in EC technology has introduced a wide variety of ECs such as pseudocapacitors and asymmetric capacitors. Along with conventional capacitors, the three categories of ECs will be elaborated.

2.2.1 *Conventional Capacitors*

Manifold forms of conventional capacitors or condensers are commercially available; however, their fundamental designs and storing mechanisms are similar. Capacitors are designed through sandwiching dielectric materials such as glass, plastic, and ceramic with two electrically conductive plates. During the charging of capacitors, a potential difference is applied across the two plates, arranging positive and negative charges in the dielectric layer accordingly as shown in **Figure 2**.

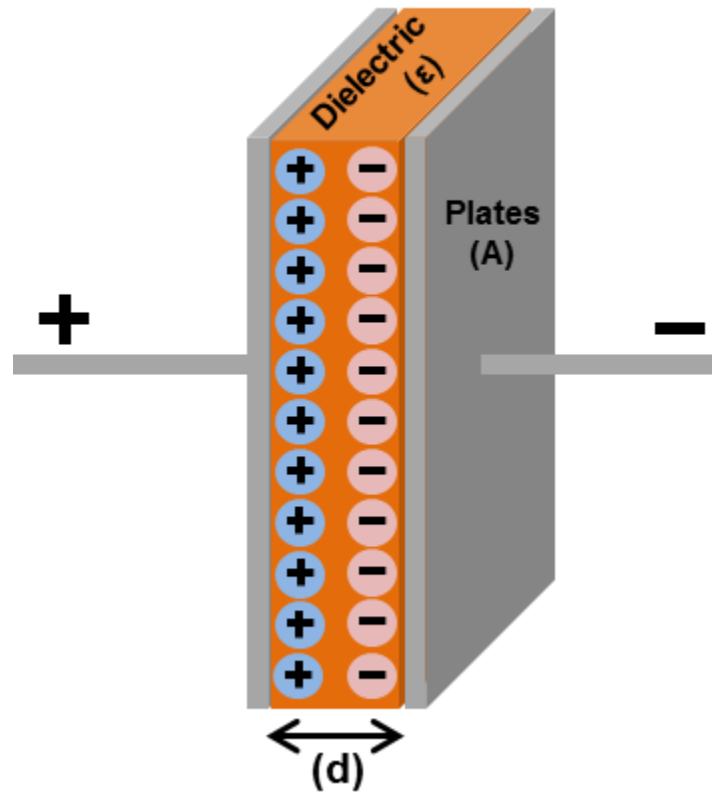


Figure 2: Charged state of conventional capacitors

Capacitance (C) is the measurement of the stored energy in charged capacitors and it is measured in farad (F). **Equation 1** is used to calculate the capacitance of a parallel-structured capacitor such as the one shown in **Figure 2**.

$$C = \frac{A * \epsilon}{d} \quad \text{Equation 1}$$

where A is the contact area of the plates, ϵ is the permittivity of the dielectric material, which measures the resistance of the material during the formation electric fields, and d is the distance between the plates. Commercially available capacitors are in the range between pico- (pF) to micro-farads (μ F).

2.2.2 Electrostatic Double-Layer Capacitors (EDLC)

EDLCs charging mechanism is similar to conventional capacitors, yet charges are stored in the interface between electrodes and electrolyte of EDLCs rather than in the dielectric layer of conventional capacitors. **Figure 3** illustrates the accumulation of ionic charges of the electrolyte in the micro pores of the electrodes when a potential difference is induced.

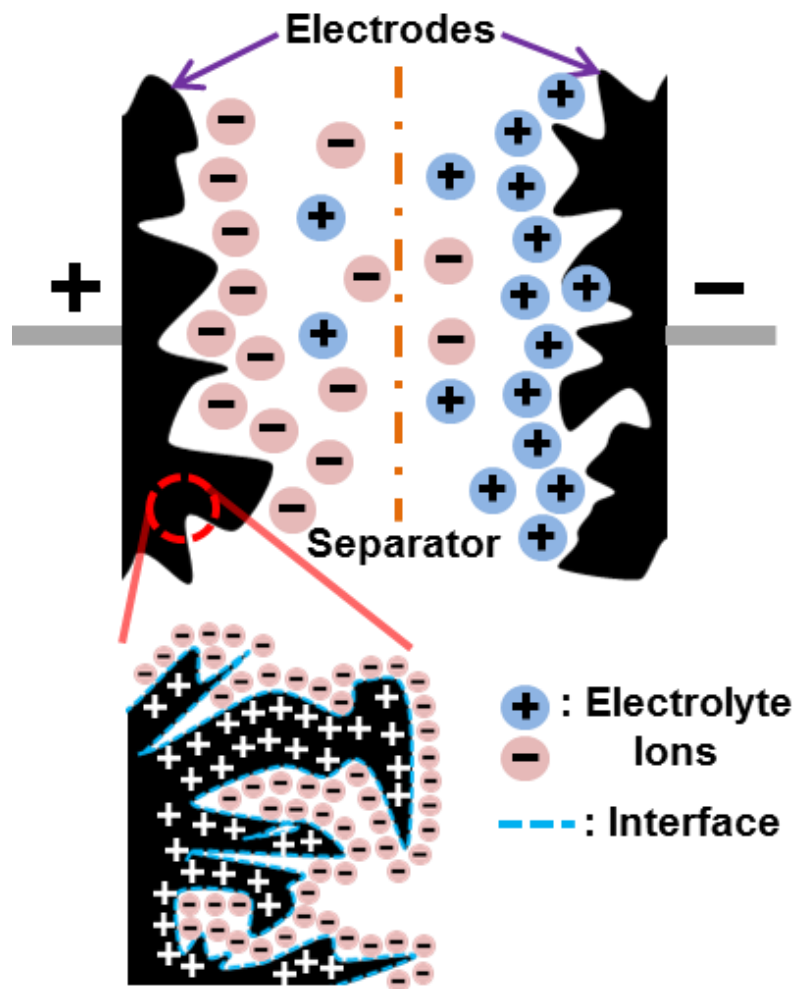


Figure 3: An accumulation of ionic charges in the interface formed between electrolyte and electrodes

Since the distance of the electrode/electrolyte interface is atomic scale, the capacitance according to **Equation 1** drastically increases, thus EDLCs exhibit exceedingly high capacitance [6]. In addition to minimizing the distance, electrodes with high surface area can boost the overall capacitance. Furthermore, excellent electrical conductivity within electrodes will minimize the internal resistance of ECs and good wettability of the electrolyte will facilitate faster mobility of ions into the pores of electrodes to further enhance the capacitive performance of EDLCs [6, 7]. An electrode material that fits into all of these requirements is carbon. Currently, electrodes of commercial ECs utilize a specific type of carbon known as activated carbon (AC). AC-based electrochemical capacitors can yield specific capacitance values of 100 to 120 F g⁻¹ in organic electrolytes [8]. More sophisticated carbonaceous materials such as carbon nanotubes (CNTs) and graphene are actively being researched for use in ECs and have shown to surpass capacitive performance of AC-based ECs. For example, Zhu *et al.* synthesized KOH-activated graphene which demonstrates a superior specific capacitance of 166 F g⁻¹ in organic electrolyte [9]. Due to scalable issues and high costs, these advanced carbons have not implemented in commercial ECs thus far.

2.2.3 *Electrochemical Pseudocapacitors*

Instead of physically storing charges as EDLCs do, electrochemical pseudocapacitors store charges through fast and reversible faradaic reactions (*e.g.* oxidation/reduction) at the surface of electrodes. The transfer of electrons during faradaic reactions of pseudocapacitors contributes 10 to 100 times more capacitance than carbon based EDLCs [10]. Ruthenium oxide is one of the most researched materials for pseudocapacitors and has exceptional

capacitive performance. Possessing multiple redox phases (*i.e.* Ru(IV)/(III) and Ru(III)/Ru(II)) in proton-rich electrolytes (*e.g.* H₂SO₄), the precious metal can undergo several electron transfers and exhibit high capacitance [6, 11]. For example, RuO₂ nanotubes synthesized by Hu *et al.* demonstrate performance on the order of 1300 F g⁻¹ in H₂SO₄ electrolyte [12]. However, the outstanding performance of RuO₂ is counterbalanced with the high cost and toxicity of the metal. Therefore, researchers have exerted effort into developing alternative pseudocapacitive materials such as non-precious transitional metal (*e.g.* cobalt oxide) and conductive polymers (*e.g.* polypyrrole). Cobalt oxide nanowires formed by Gao *et al.* display 570 to 700 F g⁻¹ [13] and polypyrrole by Zhang *et al.* demonstrates a specific capacitance value of 150 to 400 F g⁻¹ [14].

2.2.4 Asymmetric Capacitors

As the name implies, asymmetric capacitors or hybrid capacitors are composed of dissimilar electrodes. Generally, a battery-like faradaic electrode serves as the energy source and a carbonaceous electrode serves as the power source in this unique design. The main advantage of the asymmetric capacitor is the expansion of operating voltage window and the increase in energy density due to their reciprocal relationship [15]. In order to maximize the capacitive performance of asymmetric capacitors, an optimized combination of both electrodes is mandatory. Z.Wu *et al.* developed an asymmetric capacitor from MnO₂ nanowires and graphene which exhibited an energy density of 30.4 Wh kg⁻¹ while symmetrically configured capacitors yielded much lower energy density: graphene/graphene (2.8 Wh kg⁻¹) and MnO₂/MnO₂ (5.2 Wh kg⁻¹) [16]. Further improvement by incorporation of MnO₂ on a

graphene electrode with an adjacent AC nanofiber electrode by Fan *et al.* exceeded Z.Wu *et al.*'s asymmetric capacitor by more than 20 Wh kg^{-1} [17]. The structure of MnO_2 -graphene/AC capacitor is illustrated in **Figure 4**.

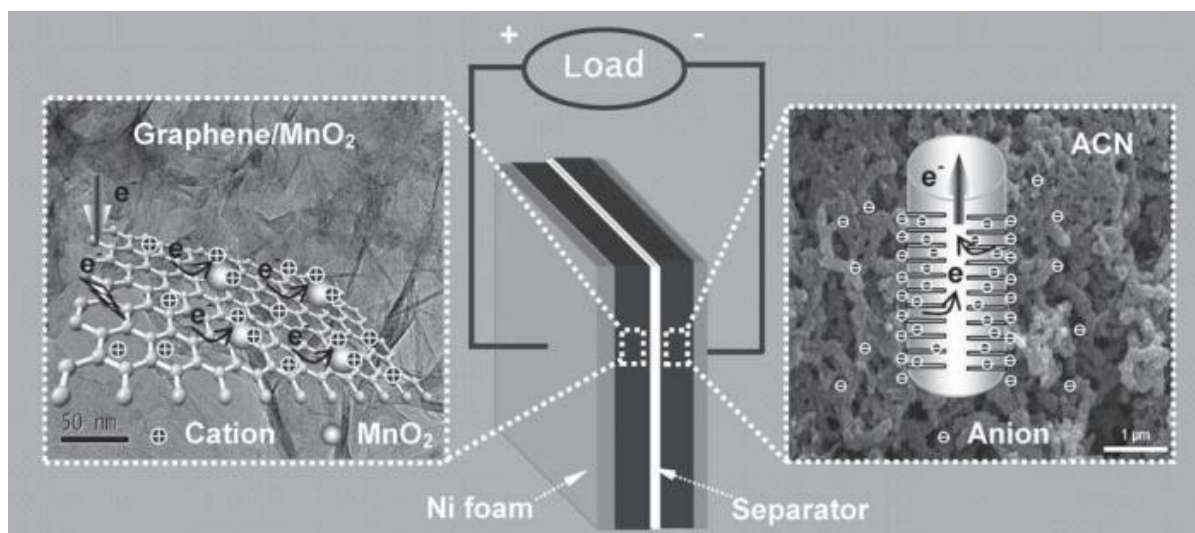


Figure 4: Schematic of an asymmetric MnO_2 -graphene/AC EC [17]. © Wiley.

2.3 Applications

Rechargeable lithium ion batteries have been and are still the dominant energy storage system in the world. However, with the increasing demand for improved energy storage for applications such as portable electronics and hybrid electric vehicles, high-powered ECs are garnering significant attention from the energy market.

2.3.1 Consumer Applications

In terms of personal electronics, cordless screw drivers powered by ECs from Coleman Company Inc. are commercially available. Becoming operational within minutes of fast

charging is the attractive property of this tool [18]. In addition, Maxwell Technologies collaborated with Celadon and invented EC-powered remote controllers which can be charged instantly while preserving the long life span of the capacitors so that ECs outlast the controllers [19]. Speakers are another example of a consumer electronic that can be powered by ECs. Sam Beck from Blueshift designed portable speakers equipped with ECs which can be fully charged within five minutes and facilitate play back at full volume for six hours [20].

2.3.2 Public Sector Application

The wind energy sector is actively looking to incorporate clear and alternative energy sources. ECs are amenable to many applications in wind energy. For example, ECs are capable of adjusting the blades of wind turbines accordingly in unpredictable weather conditions as they can supply short bursts of power to react to abrupt wind forces [21]. Additionally, the low-maintenance cost and long cycle life of ECs are suitable to be installed in unmanned wind turbines. As another example of a public sector application, Emirates Airline cable cars are equipped with ECs to support their cable car accommodations such as lights and air conditioning. During the short stops of the cable cars at their stations, the ECs are rapidly charged to power the amenities for a five-minute ride [22].

2.3.3 Public Transportation Application

The most prospective utilization of ECs involves the harnessing of brake energy from public transportation. Heavy vehicles (*e.g.* trucks) and public transportation vehicles (*e.g.* buses,

trains) make frequent stops during their operations and during each stop, enormous amounts of brake energy are released. EC's fast charging capability is ideal for capturing the brake energy. The captured energy can then be discharged back to vehicles to assist the acceleration and consequently reduce the overall fuel consumption and CO₂ emissions. This recycling of brake energy is often referred as regenerative braking and it is currently implemented in several countries. For example, one tonne of ECs were installed onto a Swiss tram to capture its brake energy and the stored energy was sufficient enough to power the tram for a short distance [23]. Similarly, trams in Paris, carrying a bank of forty-eight electrochemical capacitors on each vehicle, were capable of traveling between stations via regenerative braking energy and energy charged during the idling time at each station (~20 seconds) [24]. In terms of road side public transportation, Sinautec developed forty-one seat municipal buses powered entirely by electrochemical capacitors. The buses are capable of travelling a few miles to neighboring stops where the capacitor system is recharged during the short layovers stops. This EC-powered bus can save up to \$200,000 in fuel than relative to a commercially available diesel bus based on a vehicle's expected twelve-year life [25].

2.3.4 Future Prospective Application

Further research and development is in progress to uncover more innovative applications for ECs. For example, Volvo created a mixture of carbon-fibers and polymer resins to be used as a raw material for car components (*e.g.* car chassis). The mixture can be easily molded into desired shapes and function as ECs. This material has already been implemented into Volvo's S80 prototype by substituting it for the trunk lid and plenum cover in order to store

the brake energy [26]. A more recent breakthrough in development was the discovery of an extremely porous and high energy density graphene synthesized by a group of South Korean scientists. One gram of this material has the equivalent surface area of a basketball court, which translates into high energy density. ECs composed of this engineered graphene only require 16 seconds to fully charge while demonstrating high power capability. Nevertheless, the scale-up of this graphene production is still a barrier to commercialization [27]. For everyday life application, the concept of wearable electronics as illustrated in **Figure 5** is emerging to be more realistic as researchers are integrating EC technology into clothing.

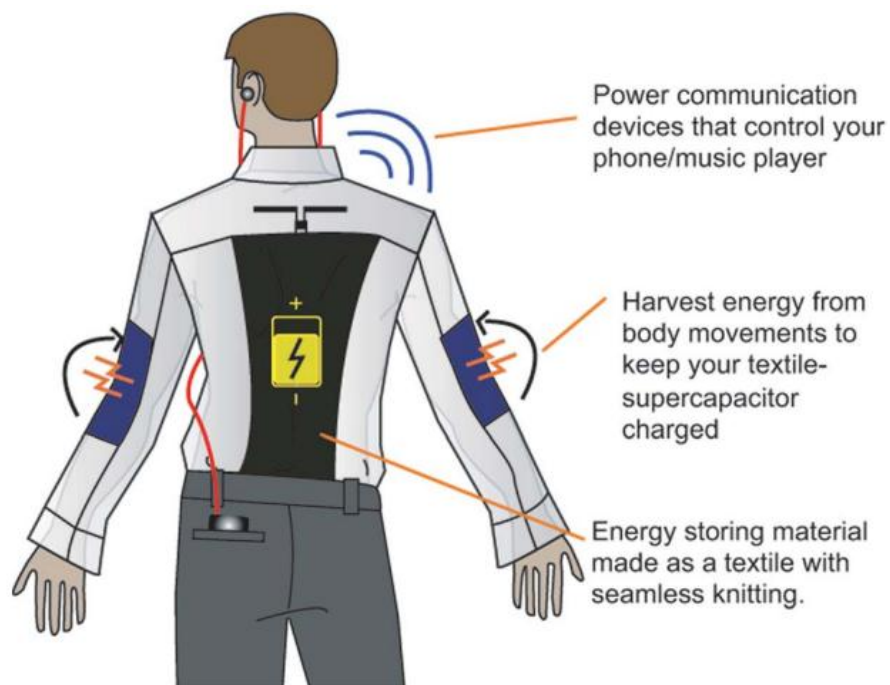


Figure 5: Concept of integrated energy storage in wearable electronics [28]. © RCS Publications.

A research group from the University of South Carolina developed a capacitive T-shirt from an ordinary T-shirt bought in a local store. Xiaodong Li from the group soaked the T-shirt in fluoride solution, and then baked it in an oxygen-free oven at a high temperature. As a result,

the surfaces of the shirt fibers transformed into activated carbon which can store charges as EDLCs [29].

2.4 Challenges and Perspectives

Despite the advantageous properties of ECs and their many prospective applications, commercialization of these capacitors is currently confined by numerous challenges. One of the major challenges for ECs is their low energy density when compared against lithium ion batteries for a given size or mass [30]. Therefore, industries and consumers are not in favor of replacing batteries with ECs. Additionally, the cost of manufacturing ECs is expensive. Currently around the world, approximately 200 lithium ion battery manufacturers are competing in the energy market to produce the best product with the lowest price. In comparison, only 80 electrochemical capacitor manufacturers are exerting effort to lower the cost of their products for them to be more attractive to customers [30]. Therefore, as of this moment, prices of ECs are more expensive than lithium ion batteries'.

Nevertheless, these challenges in the near future will be resolved as significant resources have been invested in the research and development of the EC technology. In 2013, Ioxus, an EC company, raised \$15 million worth of equity for the R&D [30]. Industries predict a rise of 19.85% for EC market at a compound annual growth rate (CAGR) through 2016 [31]. The growth in the market will hence increase the number of manufacturers and lower the price of ECs. Even now, wind energy and transportation industries are purchasing ECs for their

applications as an example \$100 million worth of electrochemical capacitors from Maxwell Technologies are sold every year.

2.5 Electrodes

Depending on the electrode materials, ECs are distinguished into EDLCs and pseudocapacitors since the charging mechanism varies by material. Despite the difference in charging mechanism, electrode materials, share a number of common properties such as:

- Excellent surface wettability
- Large surface area and high porosity
- Long cycle stability ($> 10^5$ cycles)
- High electrical conductivity
- Facile manipulation of morphology (*e.g.* pore sizes, pore distributions)
- Thermodynamic stability at operational potential range

2.5.1 EDLC Materials

Carbon's low manufacturing cost, abundance, large surface area, and high electrical conductivity are excellent properties for the material to become the dominant EDLC electrode materials. Several alterations of carbon can be classified into three categories: activated carbon (AC), carbon nanotube (CNT), and graphene.

Activated Carbon (AC)

Electrodes of commercial ECs in the current markets are composed of ACs. Generally, ACs are processed from carbonaceous precursors such as petroleum pitches, coals, woods, and hard-shells. Thermal or chemical activation, such as KOH activation, are the most popular techniques to produce ACs with low processing costs. Sufficient energy from activations breaks the linkage between small hexagonal carbon rings and deforms the structure, creating additional pores [32]. Creation of these pores increases the surface area which overall translates into high capacitive performance of ACs. For example, a specific capacitance of 100 to 200 F g⁻¹ is achievable for AC-based ECs in aqueous electrolytes [33]. Wen *et al.* achieved a specific capacitance of 225 F g⁻¹ with KOH-treated ACs in aqueous electrolytes [34].

Carbon Nanotubes (CNTs)

CNTs are engineered carbon, composed of graphitic walls assembled in near-1-dimensional cylinders (**Figure 6**). This construction allows for improved performance over ACs. CNTs are classified into two types: single-walled (SWCNTs) and multi-walled carbon nanotubes (MWCNTs).

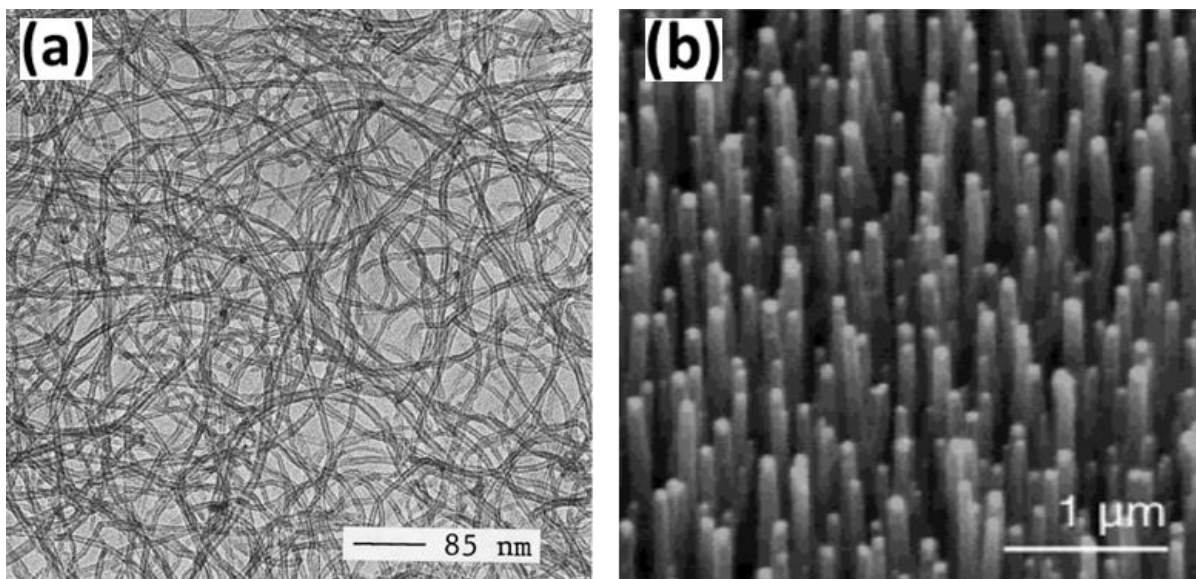


Figure 6: (a) Transmission electron microscope (TEM) image of catalytically grown carbon nanotubes [35]. © AIP Publishing. (b) Scanning electron microscope (SEM) image of carbon nanotube forests [36]. © ACS Publications.

The 1-D cylindrical structure of CNTs offers excellent mechanical properties and prevents scattering of electrons which offers great electrical conductivity [37]. Highly-ordered CNT arrays possess high surface area and large porous area for elevated capacitive performance [38]. Despite these attractive properties of CNTs, a major deterrent from the potential application of CNTs in commercial ECs is their high cost. Limited techniques, such as carbon arc discharge and chemical vapour deposition, are implemented to produce lab-scale amounts of high purity CNTs [39]. However, manufacturers are still faced with challenges of scaling up the production of CNTs with reasonable cost for commercialization.

Graphene

The discovery of flat 2-D honeycomb shaped monolayer sheets of carbon atoms, known as graphene, was a breakthrough in carbon-related scientific research. Graphene possesses

exceptional properties, such as high thermal/electrical conductivity, mechanical strength, chemical stability, and large surface area [40]. These properties have propelled a strong research interest in graphene. **Figure 7** demonstrates graphene as the essential building blocks of other carbon materials [41].

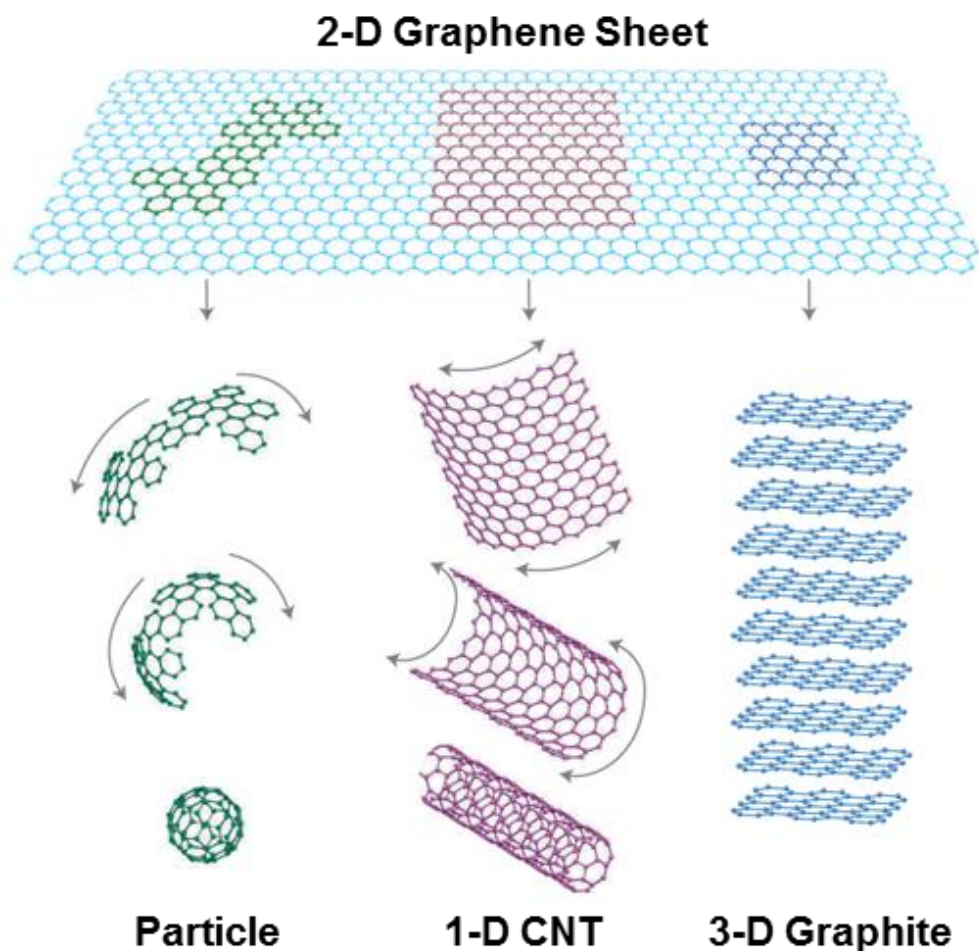


Figure 7: Illustration of 2-D graphene sheet as the building blocks for other carbon materials such as particle, 1-D CNT, and 3-D graphite [41]. © ACS Publications.

Graphene has a theoretical surface area of $2675 \text{ m}^2 \text{ g}^{-1}$ which can generate 550 F g^{-1} if all of the area is fully utilized [42]. However, agglomeration and restacking of graphene sheets limit the specific capacitance of graphene to be around 100 to 200 F g^{-1} . In order to preserve

the spaced-out structure of graphene, Wang *et al.* placed CNTs as a spacer in between graphene sheets which drastically increased the capacitance to 318 F g^{-1} (**Figure 8a**) [43]. Other techniques such as doping of graphene planes with nitrogen atoms by Hassan *et al.* increased the electrical conductivity and promoted graphene-ion interaction in electrolyte solutions [44]. The resulting nitrogen-doped graphene exhibits a capacitance value of 194 F g^{-1} (**Figure 8b**).

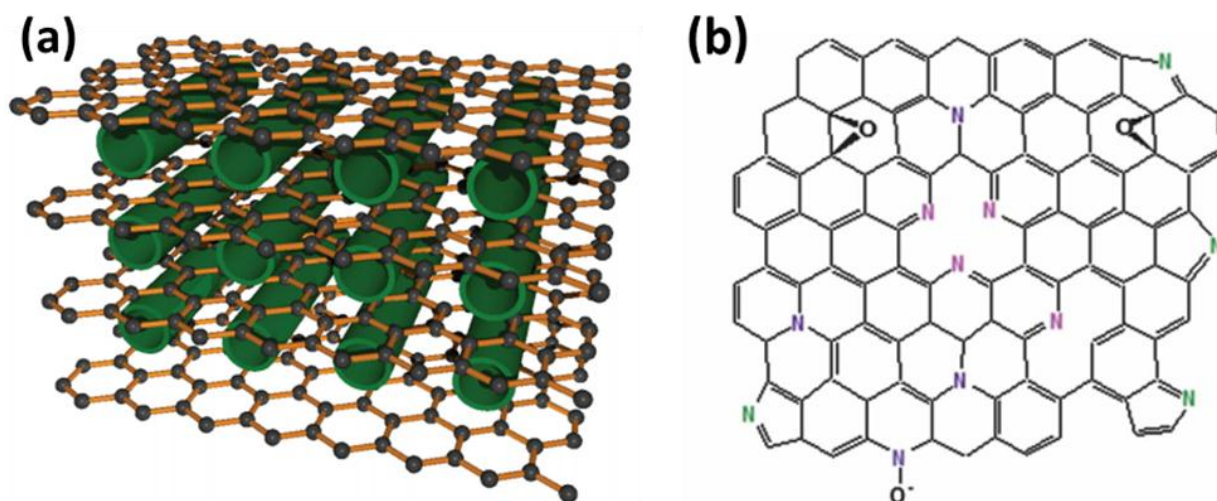


Figure 8: (a) Model of graphene sheets separated by CNTs [43]. © ACS Publications. (b) Nitrogen-doped graphene structure [44]. © RSC Publications.

2.5.2 Pseudocapacitor Materials

Common electrode materials selected for pseudocapacitors are transition metal oxides and electrically conductive polymers. These materials utilize different charging mechanisms than the static charging mechanism of EDLCs which contributes to higher energy storage and capacitive performance. However, pseudocapacitors suffer from cycling issues. Extensive cycling of these materials leads to undesirable changes in morphology and reduction in

performance. Therefore, carbon additives are often incorporated with pseudocapacitive materials to resolve the detriment.

Transition Metal Oxides

Commonly researched transition metal oxides for pseudocapacitive electrodes are RuO₂ [45], Co₃O₄ [46], MnO₂ [47], NiO [48], and V₂O₅ [49]. These metal oxides can undergo multiple oxidation states at specific potentials which increase the overall capacitance. RuO₂ is one of the most thoroughly researched metal oxides for pseudocapacitive materials due to its good reversibility, multiple oxidation states, acceptable life cycle, and high capacitive performance [8]. For example, Hu *et al.* maximized the performance of hydrous RuO₂ by annealing it in high temperature to generate a capacitance value of 1340 F g⁻¹ [50]. Unfortunately, toxicity and high cost of ruthenium metal has shifted the attention of researchers toward non-precious metals that are safer and more commercially available which include: cobalt, manganese, nickel, and vanadium oxides. **Table 1** summarizes the morphologies and the specific capacitances of the previously mentioned metal oxides and **Figure 9** illustrates each of their morphologies.

Table 1: Morphology and performance of currently researched metal oxides for pseudocapacitor applications

Compound	Morphology	Specific Capacitance (F g ⁻¹)	Reference
Co ₃ O ₄	Brush-like nanowires	1525	[51]
MnO ₂	Nanowires	~800	[52]
NiO	Nanopetals	710	[53]
V ₂ O ₅	Nanoporous network	316	[54]

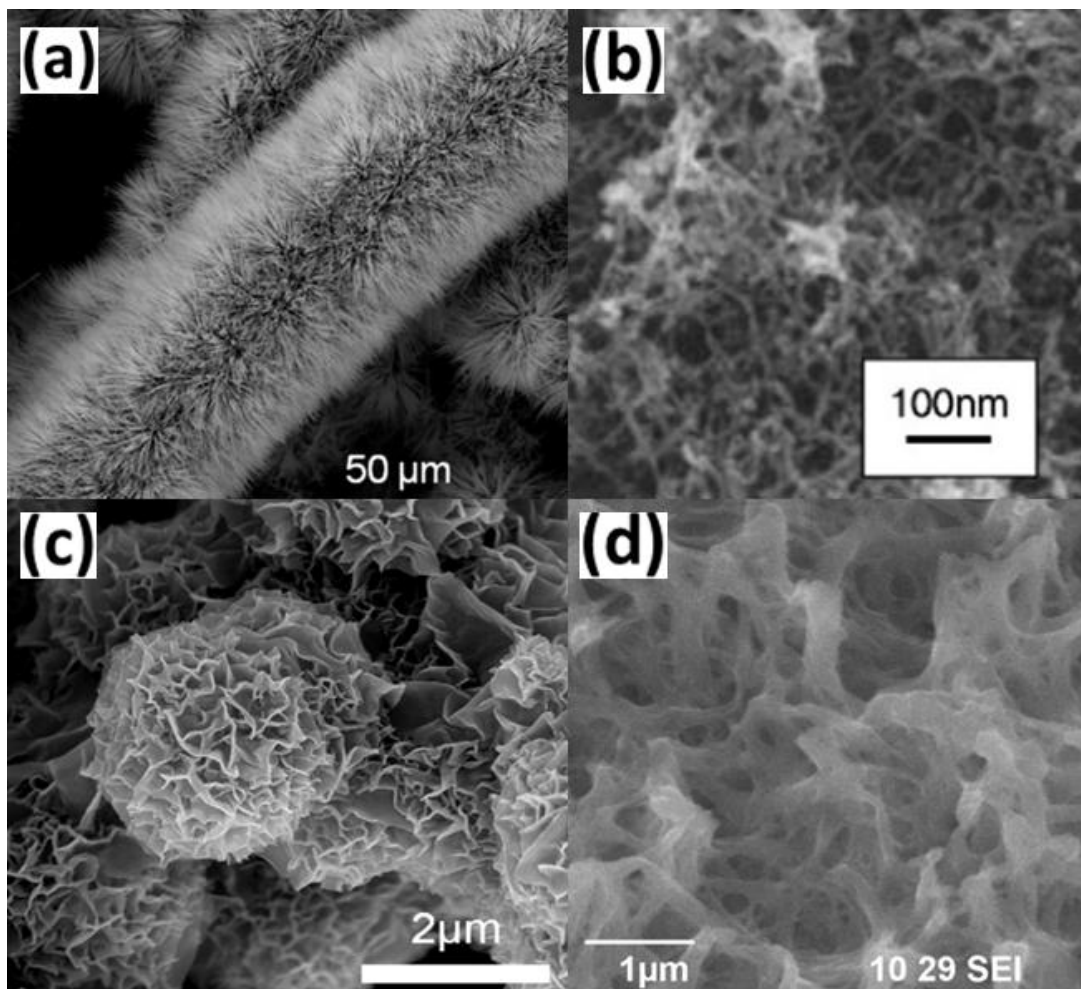


Figure 9: SEM images illustrating the detail morphologies of (a) brush-like Co_3O_4 nanowire [51]. © ACS Publications. (b) MnO_2 nanowire [52]. © Elsevier. (c) NiO nanopetals [53]. © Elsevier. (d) V_2O_5 nanoporous network [54]. © ACS Publications.

The high capacitance performances of metal oxides are compromised with low electrical conductivity which leads to loss in performance. The addition of carbon scaffolds to metal oxides can resolve this issue. As seen in the research from Li *et al.*, the MWCNT incorporated MnO_2 enhanced the capacitive performance [55].

Conducting Polymer

Electrically conductive polymers (*e.g.* polypyrrole (PPY), polyaniline (PANI)) are alternative materials for pseudocapacitors. However, these special types of polymers utilize different methods of energy storage than the faradaic mechanism of transition metals. During the charging and discharging periods, conducting polymers switch between two doping states (*p*-doping/*n*-doping) where electrolyte ions are inserted/extracted from the polymers' backbones (Figure 10) [56].

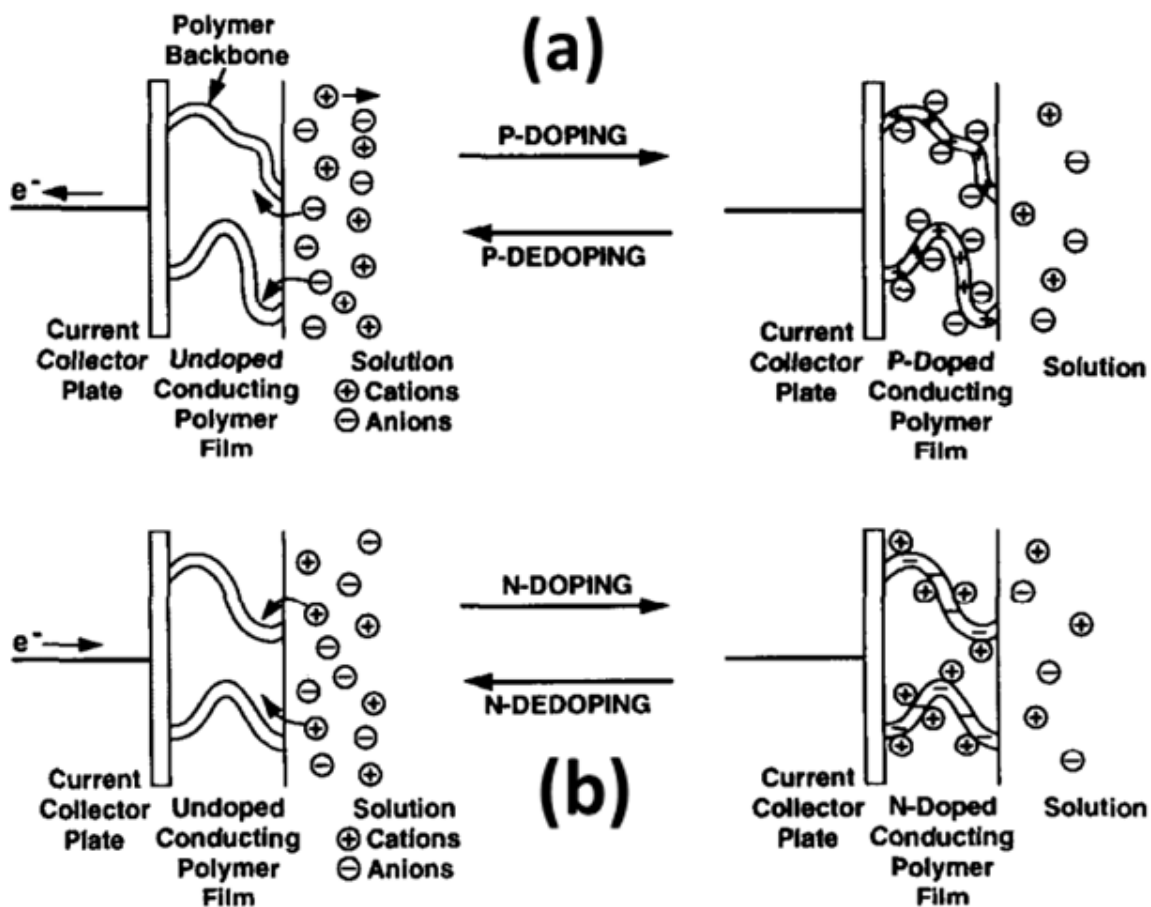


Figure 10: Illustration of conducting polymer's charging/discharging mechanism with two doping states: (a) *p*-doping and (b) *n*-doping [56]. © Elsevier.

Unlike the utilization of the surfaces of metal oxides, the entire polymer structures are exposed to the doping of ions which results in high capacitive performance. For example, PANI synthesized by Zhou *et al.* exhibited a capacitance of 609 F g^{-1} [57]. But, the immediate charge/discharge nature of ECs can induce swelling and cracking of polymer structures which ultimately shorten the polymer's overall life cycle and reduce the capacitive performance. In order to resolve this issue, carbon supports are added to conductive polymers. Wang *et al.* demonstrated an improvement in capacitance by comparing PANI-only (216 F g^{-1}) to GO-doped PANI (531 F g^{-1}) [58]. **Figure 11** displays PANI arrays on GO sheet and PPY on graphene by Xu *et al.* and Davies *et al.* [59, 60]. The specific capacitances are 555 F g^{-1} and 237 F g^{-1} , respectively.

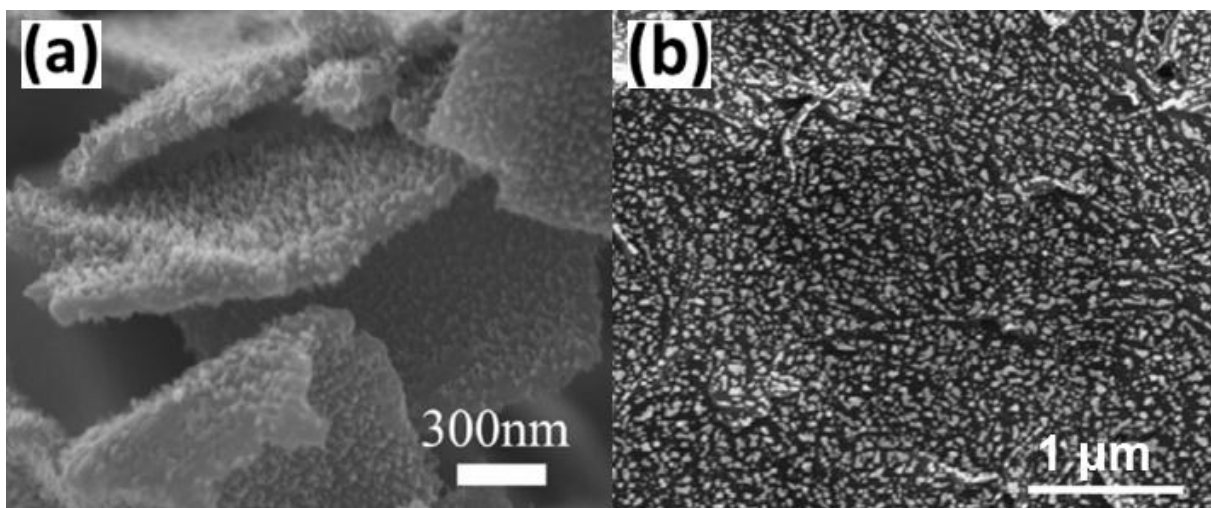


Figure 11: SEM images of (a) PANI arrays on GO sheet [59]. © ACS Publications. (b) PPY deposited on graphene [60]. © ACS Publications.

2.6 Electrolytes

Along with electrodes, electrolytes also significantly influence EC's performance, specifically affecting the cell's operating voltage window and its resistance. Energy density is proportional to the square of the voltage window; meanwhile, the ionic resistivity is inversely proportional to the cell's power capability [61]. Therefore, selecting an electrolyte which can optimize the two parameters is one way to construct high-performing ECs. Aqueous electrolyte, organic electrolyte, and ionic liquids (ILs) are the three common electrolytes available in the market. These electrolytes have different properties which are summarized in **Table 2**. **Figure 12** visually illustrates the effects of the different electrolytes on energy density and specific capacitance.

Table 2: Density, ionic resistivity, and voltage window for various electrolytes [61].

Electrolyte	Density (g cm⁻³)	Resistivity (Ω cm)	Cell Voltage (V)
KOH	1.29	1.9	1
Sulfuric Acid	1.2	1.35	1
Propylene Carbonate	1.2	52	2.5 – 3
Acetonitrile	0.78	18	2.5 – 3
Ionic Liquids	1.3 – 1.5	125 (25°C) 28 (100°C)	4 3.25

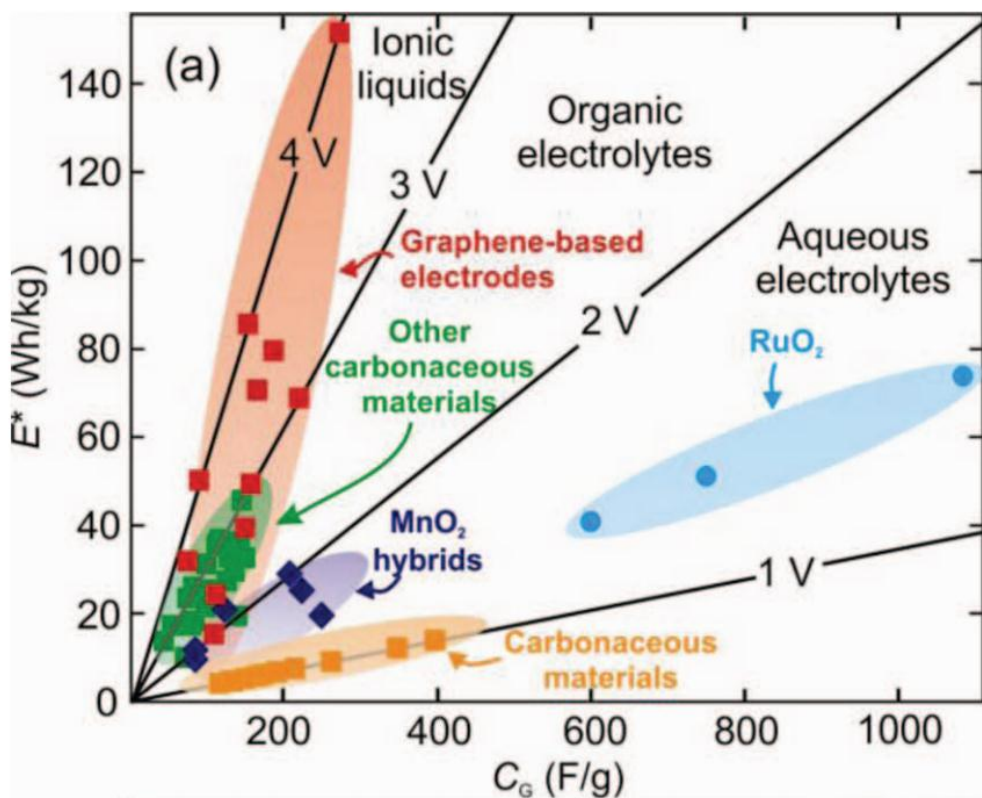


Figure 12: Illustration of energy density of two electrode cell as a function of voltage window and specific capacitance of various electrolytes [62]. © ECS Publications.

2.6.1 Aqueous Electrolytes

Aqueous electrolytes are widely used in research stages for their low cost and easy handling. Potassium hydroxide (KOH), sulfuric acid (H₂SO₄), and potassium chloride (KCl) are common aqueous electrolytes used in preliminary research stages for their low ionic resistivity, high stability in open environment, and abundance. The diversity between acid, base, and neutral electrolytes offers options for researchers to select the most appropriate electrolyte for their ECs as different electrolytes exhibit distinctive performance. For example, ECs with nickel oxide as their electrodes demonstrated an increase in performance

from 16 F g^{-1} to 155 F g^{-1} when the electrolyte was switched from H_2SO_4 to KOH , respectively since nickel oxide can only undergo faradaic reaction in an OH^- ion-rich environment [63]. However, aqueous electrolyte's narrow voltage window ($\sim 1.2 \text{ V}$) restricts the increase in energy density. Overextending the voltage window can evoke water decomposition (*i.e.* oxygen/hydrogen evolution) and build pressure within the system, leading to the rupturing of cells. Acidic and basic electrolytes with strong pH can induce corrosion on metallic components of ECs. Chloride ions from KCl can also damage the components.

2.6.2 Organic Electrolytes

Organic electrolytes can supply a wider operating voltage window (0 to $2.2 \sim 2.7\text{V}$) than aqueous electrolytes; therefore, they are employed in commercial ECs. Well-known organic electrolytes, acetonitrile and propylene carbonate (PC), offer broad voltage range which raises the energy density to the level of commercial demands. Of the two electrolytes, acetonitrile is more favourable than PC because acetonitrile's ionic resistivity is only one-third of PC's so it guarantees faster ionic transfer. Nonetheless, acetonitrile's toxicity and flammability is a concern which must be taken into an account when choosing the appropriate electrolyte. Another issue related with organic electrolytes is the aging of carbon electrodes when they are exposed to the electrolytes for long periods. Also, decomposition of organic electrolytes can occur, resulting in blockage of electrode pores [64].

2.6.3 Ionic Liquids (ILs)

ILs are mainly composed of molten salts with low melting points which are in liquid phase at room temperature. These electrolytes are non-toxic, non-flammable, and possess the widest operating voltage window (0 to 3 ~ 4 V) without any thermal or chemical instabilities [65]. Some ILs can be heated up to 300°C without vaporization [61]. The major drawback for ILs is the inadequate ionic conductivity which can reduce the performance. Heating ILs to 125°C can improve the ionic conductivity of the ILs, but other design challenges can be encountered. El-Kady *et al.* prepared laser-scribed graphene (LSG) ECs and evaluated them with aqueous, organic, and ILs electrolytes. **Figure 13** summarizes the results, where IL-based LSG EC surpasses both organic and aqueous based devices with respect to energy density and power density [66]. Although, the performance of ILs is promising, several challenges, including high costs, lie ahead for commercial applications.

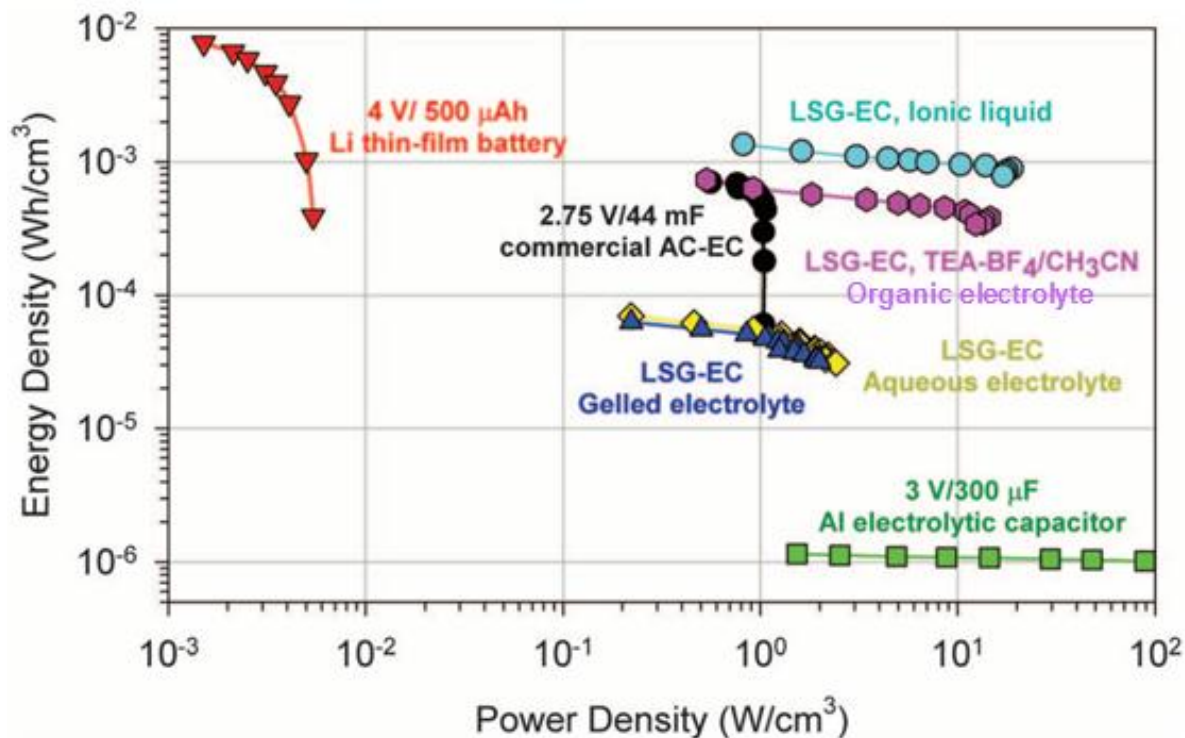


Figure 13: Illustration of energy density of two electrode cells as a function of voltage window and specific capacitance of various electrolytes [66]. © AAAS Publications.

2.7 Separators and Current Collectors

Little research has been conducted in developing well-engineered separators as many researchers have concentrated their resources in improving ECs electrodes. However, poorly designed separators can diminish the performance of ECs by generating unnecessary resistances in the cell. In a worst-case scenario, the separators can short circuit the cell. The qualifications of adequate separators for EC application include the following:

- Non-conductive (prevent electron transport between electrodes)
- Easily wetted by electrolytes
- Electrolyte-ion permeable with minimum ionic resistance

- Mechanical resistance to pressure and volume changes such as swelling
- Chemical resistance to electrolytes and electrode materials

Glass, cellulose paper, and ceramics were employed in ECs as separators in the early development stage, but the introduction of polymer-based separators dominated the separator markets for their low cost, mechanical stability, and high porosity. Two types of polymer separators, fibrous-structured separators and monolithic-networked separators, are currently used in commercial ECs (**Figure 14**).

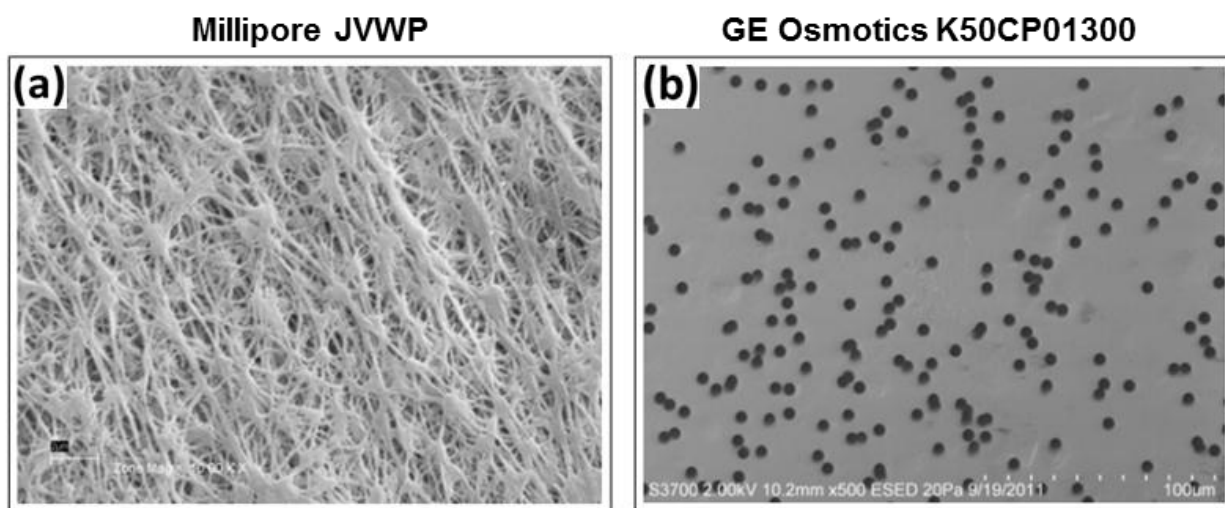


Figure 14: SEM images of (a) Millipore JVWP separator with fibrous structure and (b) GE Osmotics K50CP01300 separator with monolithic/defined pores [67]. © ECS Publications.

Apart from separators, current collectors are another important component in ECs. Their role is to transport current from electrodes to external loads with minimal loss in energy from the current collector's resistance. Therefore, current collectors must be electronically conductive and resilient in the cell environment to withstand electrolytes. With these caveats in mind, aluminum and steel are the most common choice for current collectors. To increase the contact between the electrodes and current collectors, active materials for electrodes are

directly coated onto current collectors to enhance molecular contact and to minimize interfacial resistance between active layers and current collectors [68]. Extensive cycling of ECs can damage the interfacial contact so polymeric binding agents (*i.e.* Nafion®, polytetrafluoroethylene, etc) are supplemented to the coating to inhibit dislocation of active materials from the collectors.

2.8 Physical Characterization Techniques

2.8.1 X-Ray Diffraction (XRD)

XRD is an analytical technique to identify phases of crystalline materials. In this study, XRD was used to distinguish between the two crystalline phases of nickel oxides: α -Ni(OH)₂ and β -Ni(OH)₂. XRD is based on the constructive interaction of X-rays with the sample's atoms. The X-rays are emitted from a cathode ray tube via striking a metal plate (*e.g.* copper) with highly-energized electrons [69]. As the angles between X-rays and the samples alter, the intensities of the diffracted X-rays will vary and these intensities are recorded in a pattern accordingly to the diffraction angles. The angle is also known as the Bragg angle. The XRD patterns are formed by plotting the intensity with respect to the Bragg angle. To identify the crystal structure of a material, XRD patterns are matched with the pattern of known materials. The databases for XRD patterns are vast in number and they can be easily accessed. The technique only requires less than 20 minutes with minimal amount of sample.

2.8.2 *Scanning Electron Microscopy (SEM)*

SEM was used to study the topology of the flower-shaped nickel oxides. The technique is extremely popular in observing the morphology of the surface of a sample due to instant turnaround time and simple sample preparation. SEM is capable of achieving high magnification through utilizing beams of electrons in a vacuum state and it can image the surfaces of samples on the micro and nano scale. The fundamental principle of SEM is based on the interaction of electrons with the sample. A voltage gun fires a beam of electron to the sample placed in a high vacuum chamber. The vacuum state eliminates any contaminations which can interfere with the electron beam. The beam bounces off from the sample surface and the sample-interacted electrons are collected by specifically designed electron detectors [70]. A computer then digitalizes the detected electrons into images. For clear images, samples must be conductive as the electrons maybe absorbed and charged in non-conductive materials and cause disruptive SEM images.

2.8.3 *Brunauer-Emmett-Teller (BET) Surface Analysis*

BET surface analysis technique evaluates specific surface areas of samples by employing physical adsorption of a gas on to the surface of the materials. The BET technique was used in the study to determine the surface area of the nickel oxide/hydroxide. An inert gas, mostly nitrogen, is adsorbed onto the surface and the pores. The adsorption of nitrogen takes place at a specific temperature of 77 K to form adsorption isotherm which is also known as the BET

isotherm [71]. Generally, liquid nitrogen is used to achieve the temperature. The BET isotherm deviates from the Langmuir isotherm where the BET isotherm accounts for multiple nitrogen molecules adsorbing onto given sites [72]. The principle behind measuring the surface area via BET technique is determining the number of adsorption sites on a surface as the quantitative information about the adsorption sites can be translated into surface areas [72].

2.8.4 Four-Point Probe Method

The four-point probe method is a common way to measure the resistivity of a material. The resistivity can be translated into conductivity. In this study, the method was employed to measure the conductivity of nickel oxide/hydroxide. As the name implies, the four-point probe technique requires a set-up of four probes aligned in a straight line. The two outer probes (**1** and **2**) apply current and the two inner probes (**3** and **4**) measure the voltage drop between the probes (**Figure 15**). The conductivity can be calculated using the equation below:

$$\sigma = \frac{\Delta V}{I} * \frac{L}{w * T} \quad \text{Equation 2}$$

where σ is the conductivity, V is the voltage drop, I is the current applied, L is the length between the two inner probes, T is the width of the sample, and t is the thickness of the sample. To apply this technique for powdered samples, a rectangular pellet needs to be made by using a hydraulic press and a mold.

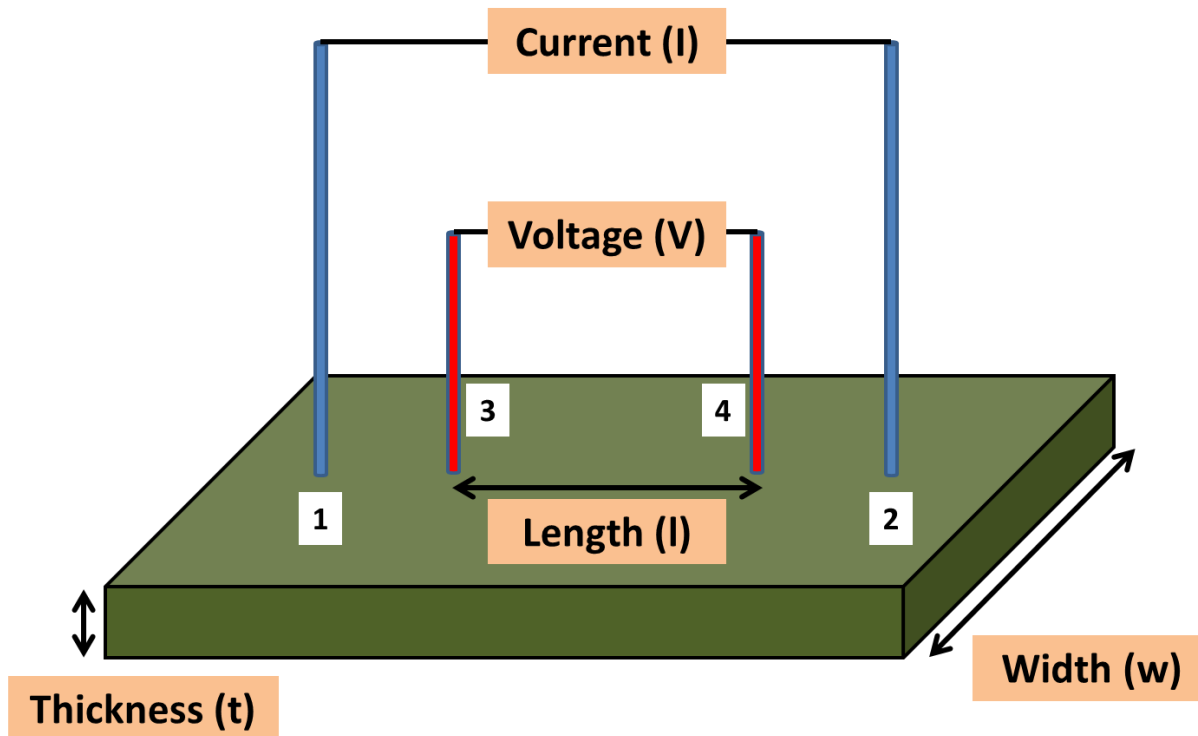


Figure 15: Schematic of the four-point probe technique

2.9 Electrochemical Characterization Techniques

2.9.1 Electrochemical Cell Design

For electrochemical testing of ECs, two testing configurations are available: three-electrode and two-electrode systems. The formal testing configuration evaluates the performance of electrode materials with minimal amounts, whereas the latter system tests the performance of fully assembled ECs.

Three-Electrode System

The three-electrode system consists of three components: (a) a working electrode, (b) a reference electrode, and (c) a counter electrode (**Figure 16**). The components are connected to a potentiostat which collects the electrical signals for analysis.

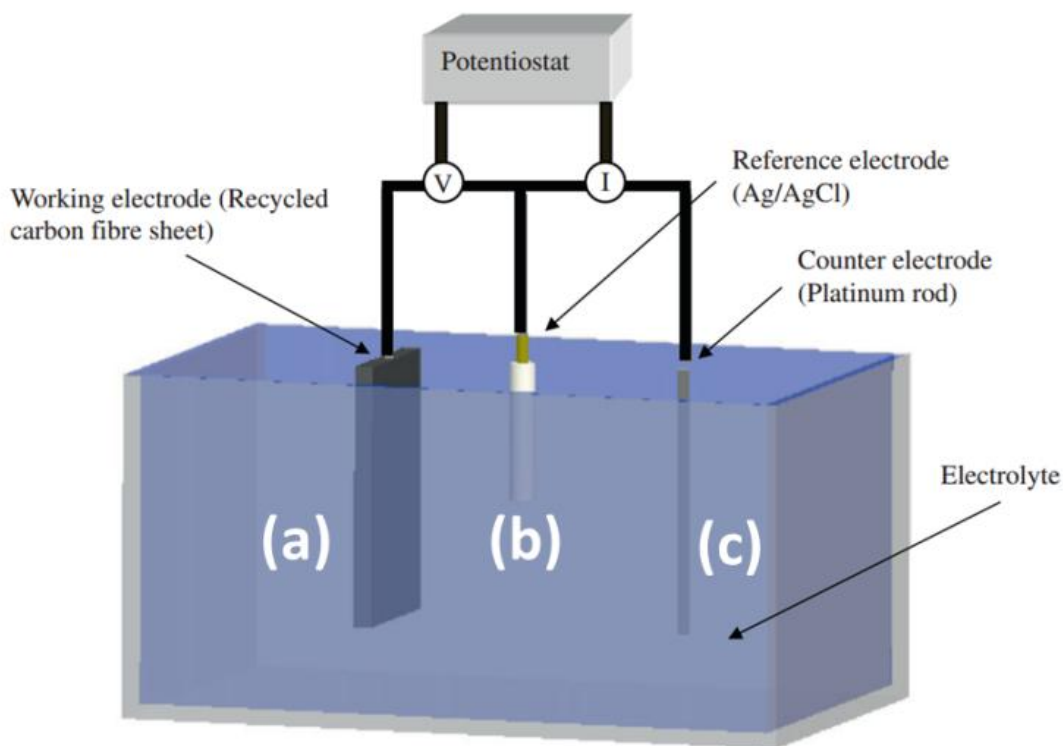


Figure 16: Schematic drawing of three-electrode system: (a) working electrode, (b) reference electrode, and (c) counter electrode [73]. © Elsevier.

The working electrode is prepared by coating the surface of a stable electrode (*e.g.* glass carbon or platinum metal) with an active material. A uniformly dispersed ink with active materials in solvents (*e.g.* water, ethanol, isopropanol) is pipetted onto the surface of a pre-polished electrode. Frequently, carbons and polymeric binders are added into the ink to enhance the conductivity and to prevent diffusing of the coating in the electrolyte. The reference electrode serves as a reference potential by providing a pre-defined and fixed

potential. Many different types of reference electrodes exist: normal hydrogen electrode (NHE), silver chloride electrode (Ag/AgCl), and saturated calomel electrode (SCE). Finally, the counter electrode serves as a balancing electrode which complements the reaction occurring in the working electrode by adjusting its potential. For this purpose, highly conductive and chemically stable materials such as platinum meshes or graphitic rods are chosen.

Two-Electrode System

The two-electrode system, also referred to as the full-cell system, involves the testing of two active electrodes: a cathode and an anode. **Figure 17** illustrates a schematic of this system.

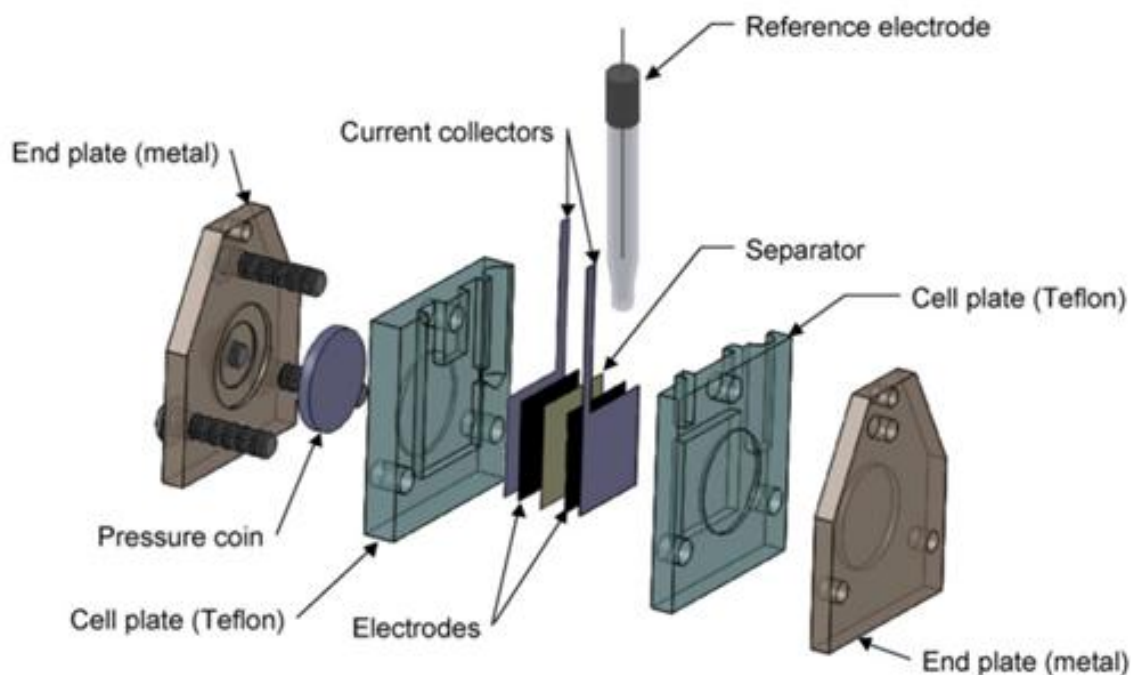


Figure 17: Illustration of a two-electrode system [74]. © Elsevier.

A separator in between the two electrodes prevents short circuiting. Metal plates serving as current collectors adjoin the two electrodes and the separator. Metal end plates encase the components with screws to apply even pressure throughout the cell. Prior to testing of the cell, it is submerged in electrolyte long enough for the pores of the electrodes to be saturated with the electrolyte. Anodes and cathodes are fabricated by pasting or spraying uniformly dispersed ink with active materials and solvents onto stable carbonaceous sheets (*e.g.* carbon paper, carbon fiber). The sheets can be further trimmed to desired dimensions. A reference electrode can be placed in the cell to measure the potential of individual electrodes.

2.9.2 *Cyclic Voltammetry (CV)*

CV is one of the most widely used techniques to evaluate quantitative and qualitative capacitive performance. A working electrode's potential is linearly swept back and forth between two pre-defined potentials with respect to the reference electrode's potential. Simultaneously, the current (*I*) in response to the changing potential (*V*) is collected and plotted to form a CV curve (**Figure 18**).

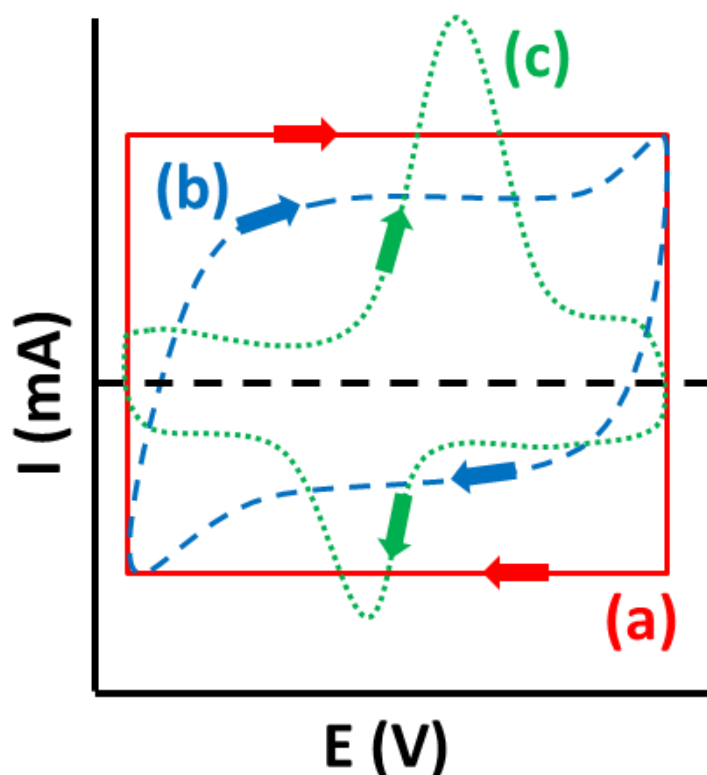


Figure 18: CV curves of (a) ideal capacitor, (b) EDLC, and (c) pseudocapacitive materials.

For an ideal capacitor, a theoretical rectangular CV curve as shown in **Figure 18a** should be observed; however, EDLC materials tend to deviate from this ideal behaviour, resulting in a deformed rectangular shape as displayed in **Figure 18b**. On the other hand, pseudocapacitors show peaks in their CV curves which represent their faradaic reactions (**Figure 18c**). From these curves, capacitance of the electrode material can be determined via **Equation 3**.

$$C = \frac{\int i dV}{2V_s V_R} \quad \text{Equation 3}$$

where $\int i dV$ is the integrated area under the CV curve, V_s is the scan rate, and V_R is the potential range. Dividing the capacitance by the mass of the active materials calculates the specific capacitance (C_s) (**Equation 4**).

$$C_s = \frac{C}{m} \quad \text{Equation 4}$$

where C is the calculated capacitance from the **Equation 3**, and m is the mass of the active material. In addition, the effect of scan rates on capacitance is significant. At lower sweeping rates, (*e.g.* 0.005V/s), the CV curve is nearly rectangular whereas the distortion of the rectangular curve is visible at higher scan rates because the electrochemical kinetics cannot contend with the rapid change in potential (**Figure 19**). Decline in capacitive performance is expected at high scan rates due to the sluggish transportation of ions and the underutilized micro pores in active materials.

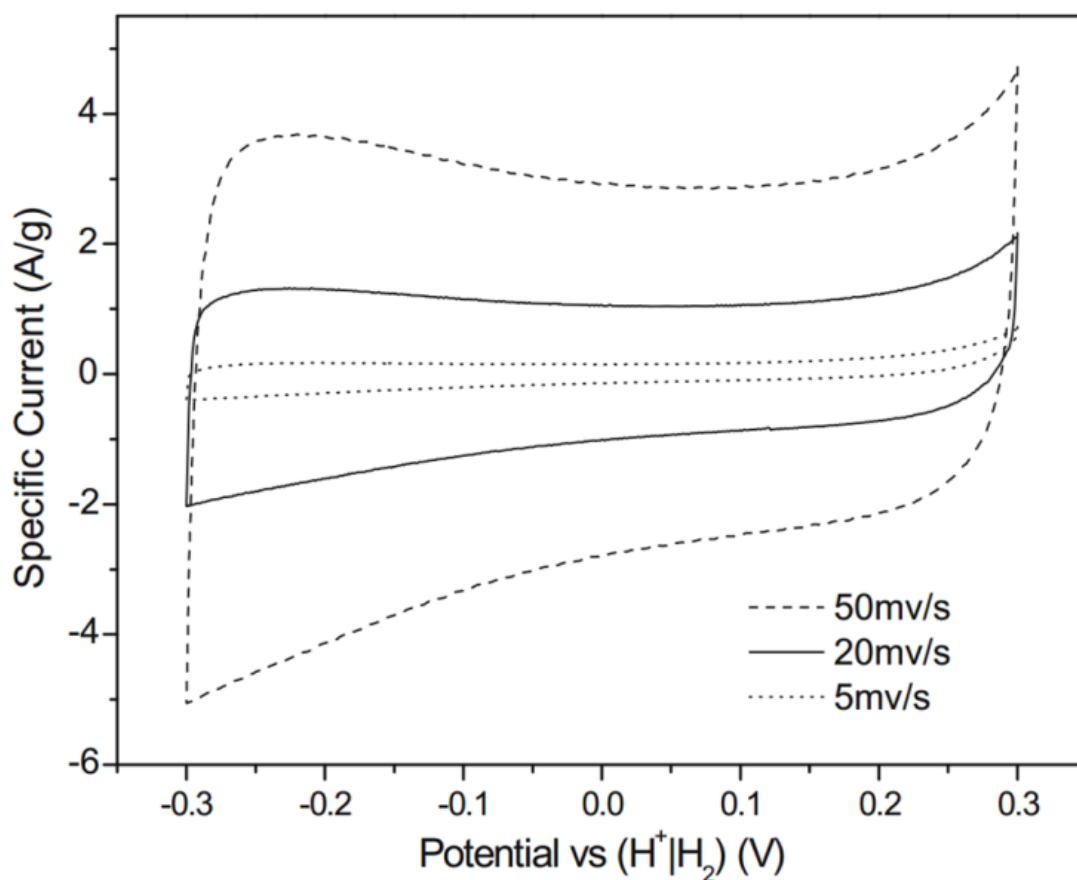


Figure 19: CV curve of ordered graphitic mesoporous carbon at different scan rates [75]. © Elsevier.

2.9.3 Galvanostatic Charge-Discharge (GCD)

In addition to the CV technique, the capacitance of ECs can be determined by another technique known as Galvanostatic charge-discharge (GCD). The technique involves applying a constant current density (*e.g.* A/g) to a working electrode and measures the responsive potential with respect to time. Basically, the electrode is charged to a certain potential and discharged back down to the initial potential; the charging and discharging processes are plotted and the curve is analyzed (**Figure 20**).

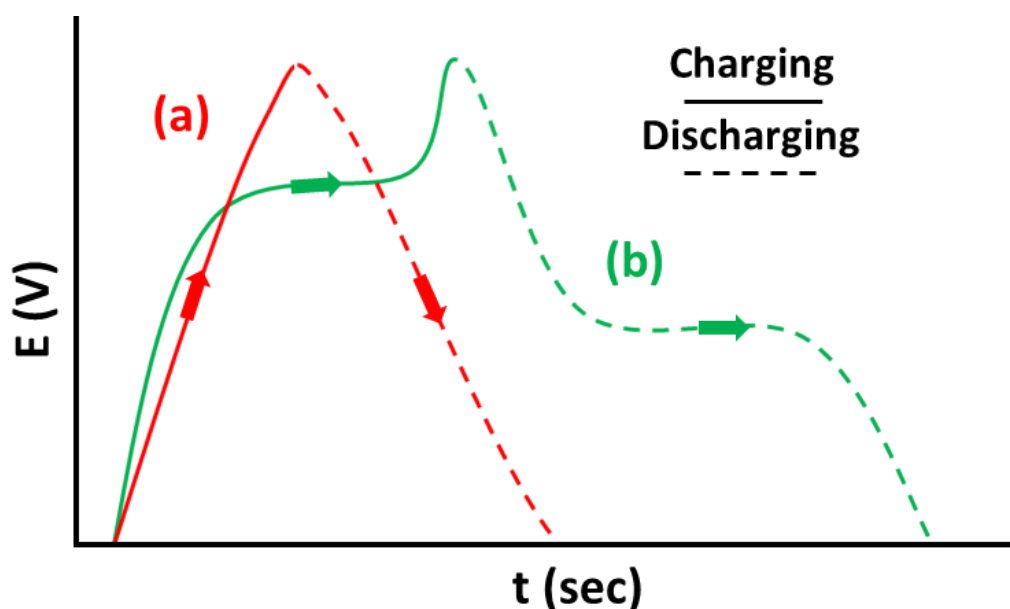


Figure 20: GCD plots of (a) EDLC and (b) pseudocapacitive material.

Figure 20a shows the linear charging and discharging curve of EDLC materials. Conversely, pseudocapacitive materials exhibit non-linear behaviour due to their redox reactions (**Figure 20b**). The discrepancy between the curves indicates that a unique equation is needed for each

type of materials in order to calculate their capacitance. For EDLC, the slope of discharging is accounted in the calculation of capacitance as shown in **Equation 5**.

$$C = \frac{I}{dV/dt} \quad \text{Equation 5}$$

where C is the capacitance of the material, I is the applied current, and dV/dt is the slope of the discharging GCD curve. For pseudocapacitive material, an altered form of equation 5 involving the total discharge time instead of the slope is utilized.

$$C = \frac{(\Delta t)(I)}{\Delta V} \quad \text{Equation 6}$$

where Δt is the total discharge time and ΔV is the potential difference at the discharging phase. To calculate the specific capacitance, **Equation 4** can be used again. Similar to the effect of scan rates on the capacitive performance, different magnitudes of current densities also influence the performance. High current densities induce insufficient utilization of pores on the surfaces and hindrance of electrochemical kinetics.

2.9.4 *Electrochemical Impedance Spectroscopy (EIS)*

EIS technique offers insight about resistances in ECs. The technique involves supplying an alternating current to ECs over a frequency range of 0.01 Hz to 1 MHz. The resulting response of the frequency is charted to form a Nyquist plot, which plots imaginary resistance (Z'') against real resistance (Z'). Various information can be extracted from the Nyquist plot. The equivalent series resistance (ESR), which is comprised of resistances from cell components (*e.g.* electrolyte resistance and contact resistance between current collectors and electrodes) [11, 76], can be evaluated by locating the intersection of the impedance curve and

the x-axis. **Figure 21** illustrates ESR of (a) ideal capacitor and (b) ECs. A deviation between ideal capacitors and ECs is seen at low frequency due to equivalent distributed resistance (EDR). EDR is the ionic resistance of electrolyte within the pores of the electrodes [11, 77]. As a result, an increase in the number of pores in electrodes will raise the EDR. The low frequency region is also referred as a Warburg diffusion regime. The regime is strictly controlled by diffusion. For an ideal capacitor with no limited diffusion control, a vertical line is observed. But for the non-ideal ECs, the line in the Warburg regime is angled. Often, the complex EIS curves are fitted with a circuit modeling software to extract more information.

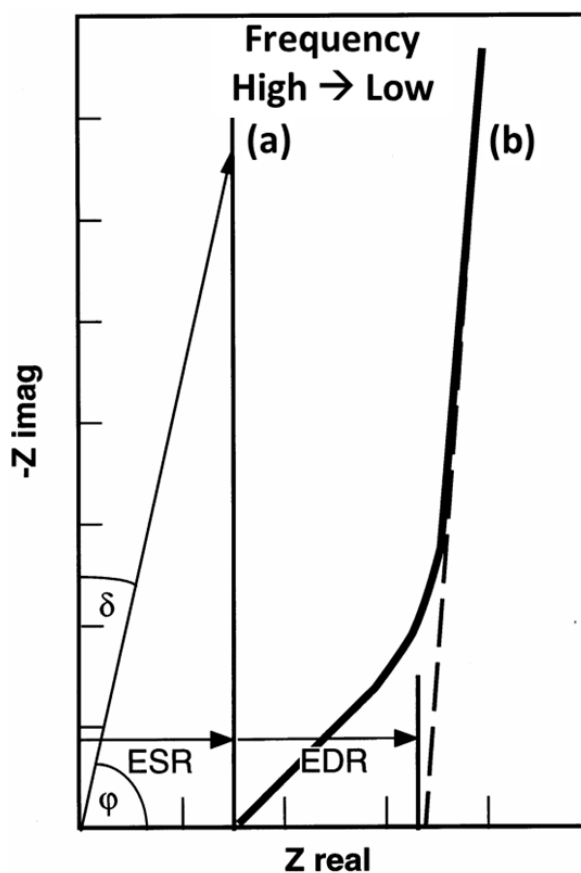


Figure 21: Schematic representation of the Nyquist plot of (a) an ideal capacitor and (b) an EC [77]. © Elsevier.

2.9.5 Energy Density and Power Density

Assessing the energy density and power density of ECs is imperative in diagnosing their deliverable performance in real-life applications. Both CV and GCD techniques can determine energy and power density.

Specific energy density (Wh kg^{-1}) can be calculated from **Equation 6**.

$$\text{E. D.} = \frac{1}{2} C_s (V_R)^2 = \frac{1}{2} \frac{C}{m} (V_R)^2 \quad \text{Equation 6}$$

where C_s is the specific capacitance from CV or GCD techniques, and V_R is the operating potential range. The latter part of the equation correlates capacitance and mass of active materials to specific energy density. The squared relationship of the operating potential term to the energy density indicates that the operating potential window has the dominant effect on the energy density. As discussed in the Chapter 3.2, electrolytes contribute mostly to the operating potential window. Therefore, selecting electrolytes with a wide operating window (*e.g.* organic electrolytes and ILs) can definitely enhance the energy density.

Specific power density (W kg^{-1}) is defined by how quickly a device can deliver its energy under a constant current density to external loads. The calculation of maximum specific power density involves ESR.

$$\text{P. D.}_{\text{Max}} = \frac{(V_R)^2}{4mR_{\text{ESR}}} \quad \text{Equation 7}$$

where V_R is the potential range, m is the mass of the active materials, and R_{ESR} is the ESR within the cell. Previously, organic electrolytes and ILs are mentioned to increase the operating voltage window and subsequently enhance the energy density. However; as a trade-off, inferior ionic conductivity of these electrolytes will increase the R_{ESR} and reduce

the overall power performance. Average specific power density can be calculated through applying a lucid relationship between specific energy density and the rate of discharge of the cell (Δt).

$$P. D._{Avg} = \frac{E. D.}{\Delta t} \quad \text{Equation 8}$$

Plotting the specific power density against its specific energy density forms a Ragone plot which provides an overview of the performance in terms of energy and power. As seen with **Figure 1** which illustrates a Ragone plot of popular electrochemical energy storage devices, a trend of diminishing power density with increasing energy density is evident with all devices.

2.9.6 Cycle Stability

Another important aspect of ECs is their cycle stability. ECs are well-recognized for possessing long life cycles with minimal degradation in performance. In lab-scale, preferably 1000 to 10,000 cycles are conducted to investigate the potential cycle durability. A cycle equates to one charge and discharge process at a constant current density; as a result, GCD technique is employed. Extensive cycling will generally degrade the electrodes and induce corrosion in the components of a cell, resulting in performance loss. To acquire foresight on how the material will perform in real ECs, the initial and the final performance is compared and analyzed. Moreover, it is known that EDLCs which utilize a static charging mechanism tend to have better cycle stability than pseudocapacitors. Chen *et al.* have demonstrated faster degradation of capacitive performance with pseudocapacitive MnO₂-deposited CNT-sponge

compared to pure CNT-sponge [78]. **Figure 22** illustrates that only a 2% drop in performance retention is observed with CNT-sponge over the course of 100,000 cycles whereas, a 4% reduction in capacitance was seen with MnO₂-CNT-sponge after 1/10th of the previous cycling conditions. The loss in performance for MnO₂-CNT-sponge would be severe if it continued until the 100,000th cycle.

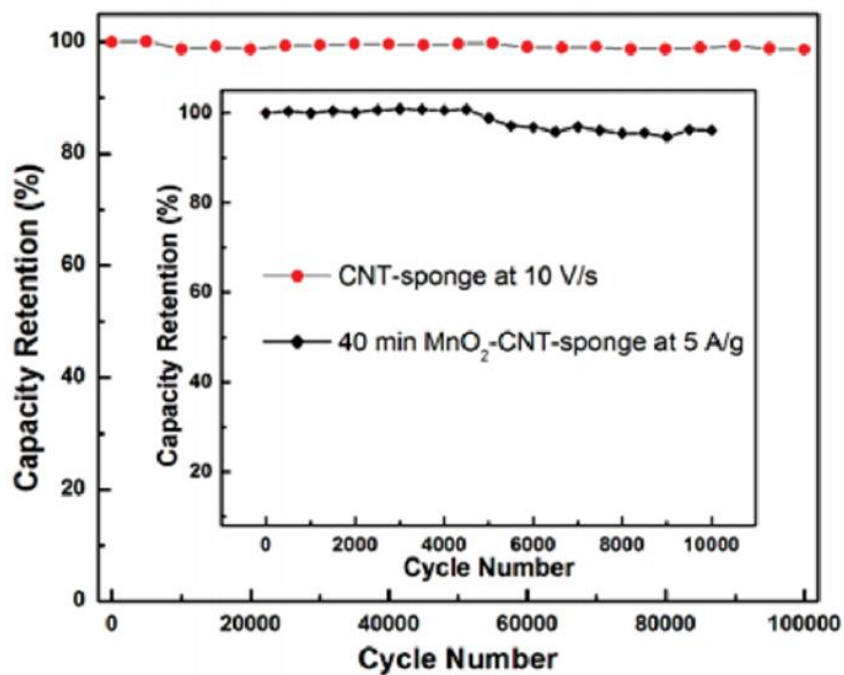


Figure 22: Performance retention versus cycle number for CNT-sponge and MnO₂-CNT-sponge [78]. © ACS Publications.

Chapter 3: Nickel Hydroxide/Oxide Hybrid Flower Structure

3.1 Introduction and Motivation

Recapping the background covered in this thesis, ECs with their unique properties, such as long cycling lifetime, high power density, and low maintenance cost, are being extensively researched to bridge the gap between high-power density conventional dielectric capacitors and high-energy density lithium ion batteries [60, 79-81]. Therefore, ECs exhibit potential for providing instantaneous and uninterruptable power for a range of applications from portable electronics such as cellular phones to new generation hybrid electric vehicles [82, 83]. ECs are broadly divided into EDLCs and pseudocapacitors based on their charge/discharge mechanisms [84, 85]. EDLCs store charges at the interface between the electrode and electrolyte according to the fast transportation of ions, whereas pseudocapacitors utilize the reversible faradaic reaction participating on the surface of the electroactive material [86, 87]. The major advantage of pseudocapacitance is the high energy transfer during the faradaic reaction, providing 10 to 100 times more capacitance than EDLCs [88]. Transition metal oxides, such as IrO_2 and RuO_2 with various oxidation states, have been researched because they are suitable candidates for pseudocapacitive materials [89, 90]. Despite the high capacitance value of 550 F/g and 1580 F/g for hydrous IrO_2 and RuO_2 , respectively, these metal oxides are toxic and costly [12, 91, 92]. Therefore, researchers have shifted their attention toward inexpensive metal oxides, including NiO [93, 94], MnO_2 [95, 96], and Co_3O_4 [97, 98]. Among the metal oxides investigated, NiO has become a popular pseudocapacitive material for ECs due to its a high theoretical capacitance value of 2573 F/g,

low cost, distinct redox reaction, and a controllable [99-101]. In addition to NiO, Ni(OH)₂ is also used for EC applications. Jiang *et al.* have successfully synthesized a thin flower morphology of α -Ni(OH)₂ with a remarkable capacitance value of 1715 F/g at a low scan rate [102].

In our research, we have successfully synthesized a flower structured NiO/ α -Ni(OH)₂ hybrid composite by tailoring the calcination period. In the process of our research, it was discovered that the hybrid composite outperforms pure NiO and α -Ni(OH)₂ individually. The hybrid composite without any carbon supports demonstrated a capacitance of 474 F/g even at a very high current density of 10 A/g.

3.2 Experimental Procedures

3.2.1 Synthesis of Nickel Hydroxide/Oxide Hybrid

Analytical grade Ni(NO₃)₂·6H₂O (Sigma-Aldrich), urea (EMD Chemicals), sodium dodecyl sulfate (SDS, Sigma-Aldrich) were used as purchased. To synthesize α -Ni(OH)₂, a solvothermal method from Beach *et al.* [103] was followed. 0.582 g Ni(NO₃)₂·6H₂O, 1.20 g urea, and 0.10 g sodium dodecyl sulfate (SDS) were magnetically stirred in 10 mL double deionized water (DDI) water and 10 mL ethanol at room temperature for 30 minutes to obtain a homogeneous solution with light green colour. The solution was then transferred to a Teflon-Lined autoclave with a stainless-steel shell where the solution was heated at 110°C for 15 hours. The product was washed three times with DDI and two times with acetone

through centrifugation and oven dried at 60°C to remove any leftover acetone. The finished α -Ni(OH)₂ was exposed to heat in air at 250°C for durations of 40 min, 2 hr, and 4 hr to control the conversion of α -Ni(OH)₂ into NiO. The heating rate from room temperature to 250°C was 10°C/min. The samples are denoted with respect to their calcination period: NiO-0min, NiO-40min, NiO-2hr, and NiO-4hr.

3.2.2 *Physical Characterization*

The synthesized materials were characterized with multiple techniques. X-ray diffraction (XRD) was performed using a Bruker AXS D8 Advance with Cu K α radiation with a wavelength of 0.154 nm to identify NiO and α -Ni(OH)₂ in the samples. A scanning electron microscope (SEM, LEO FESEM 1530, 20 eV) was used to examine the surface morphology of the nickel compounds. Brunauer-Emmett-Teller (BET) surface analysis was carried out using an Autosorb from Quantochrome Instruments to determine the surface areas and the pore classification of the materials. Rectangular pellets of NiO-0min, NiO-40min, NiO-2hr, and NiO-4hr for electrical conductivity measurements were formed by cold pressing at 40 MPa. The approximate dimensions of the pellets were 0.8 cm in width, 2.5 cm in length, and 400 μ m in thickness. The resistivity of the pellets was measured by a versastat mc potentiostat from Princeton Applied Research while implementing four-point probe technique at room temperature.

3.2.3 *Electrochemical Characterization*

Electrochemical measurements such as cyclic voltammetry (CV), galvanostatic charge discharge (GCD), and electrical impedance spectroscopy (EIS) were performed using a versastat mc potentiostat from Princeton Applied Research. The three-electrode testing method was used with a platinum counter electrode, a working electrode, and a saturated calomel electrode (SCE) as a reference electrode in 2M KOH electrolyte. The potential varied from 0 to 0.45 V vs SCE. The working electrode was prepared by adding 20 μ L of sonicated solution (1 mg/mL) dropwise onto a 5 mm OD glassy carbon. The sonicated solution is composed of nickel compounds and 1:1 ratio of ethanol and water.

3.3 Results and Discussion

3.3.1 *XRD Characterization*

Figure 23 shows the XRD patterns of the uncalcinated nickel hydroxide, NiO-0min, and Ni compounds calcinated for three durations at 250°C: NiO-40min, NiO-2hr, and NiO-4hr. The specific temperature was chosen because water can be removed from nickel hydroxide to form NiO at 250°C [104, 105]. It was found however that not all of the samples were completely into NiO. Depending on the duration of the calcination, the composition of the resulting nickel composites varied. The XRD result illustrates that the sample exposed to heat for four hours fully converted into NiO with peaks observed at 36.5, 42.7, and 61.8 degrees. Alternatively, the sample which was not calcinated (NiO-0min) remained free of

NiO, displaying diffraction peaks located at 12.4, 24.6, 33.1, and 58.9 degrees, indicating the alpha structure, α -Ni(OH)₂ [106]. The other two samples, NiO-40min and NiO-2hr, were exposed to 250°C, however only a portion of the α -Ni(OH)₂ was converted to NiO. Instead, α -Ni(OH)₂ and NiO coexist in NiO-40min and NiO-2hr with both peaks evident in their spectrum. Examining the intensity of the XRD peaks reveals that NiO-2hr has more NiO than NiO-40min, which is expected since extended calcination can remove more water, leading to a greater fraction of NiO in NiO-2hr than in NiO-40min.

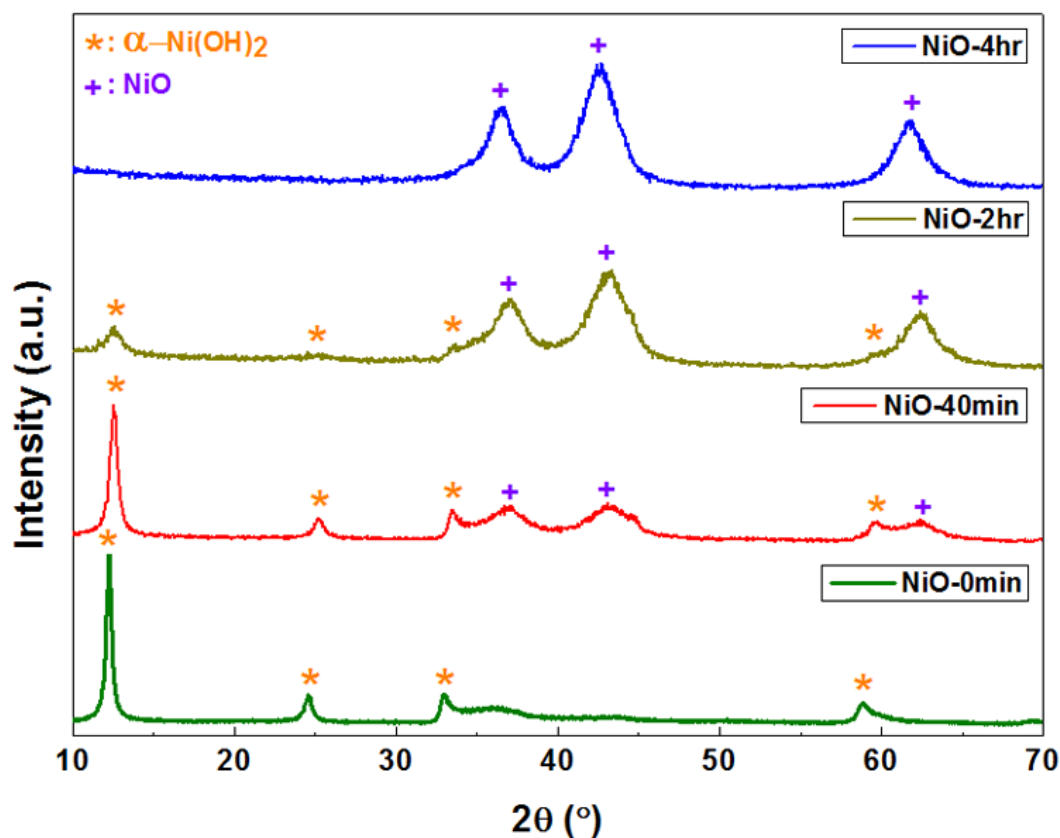


Figure 23: XRD patterns of NiO-0min, NiO-40min, NiO-2hr, and NiO-4hr [107]. © Elsevier

3.3.2 SEM and BET Characterization

The SEM images of these samples reveal flower morphology for all samples as shown in **Figure 24**. The images illustrate a spherical topology of these materials. **Figure 24A** and **24B** also display flower structure of NiO-0min. This denotes that the flower morphology, including the rippled surfaces, is formed during the synthesis of the α -Ni(OH)₂. Moreover, even after the exposure to 250°C, the nickel composites maintained their structures, signifying the structures' strong resilient to heat (**Figure 24C – H**). The exact mechanism for the formation of the flower morphology is not clear as many parameters such as hydrogen bonding, Ostwald ripening, intrinsic crystal contraction, and more contribute to the development of the morphology [105]. Earlier studies [105, 108, 109] suggest that the SDS surfactant encapsulates the Ni⁺ atoms, and the OH⁻ ions from urea react with the SDS-coated Ni⁺ atoms to form thin flakes of α -Ni(OH)₂. Then, the α -Ni(OH)₂ flakes self-assemble to form the flower morphology [105, 109]. The disordered rippled surfaces of the flower morphologies provide a larger surface area and porosity than other morphologies such as spherical particles with smooth surfaces [106]. Moreover, the flower morphology grants sufficient interspaces between the particles for easy volume expansion and enhancement of surface areas [102]. From **Figure 24**, NiO-40min, NiO-2hr, and NiO-4hr, seem to be more porous than NiO-0min because more gaps are visible for calcinated samples than NiO-0min. The calcination process removes the moisture from α -Ni(OH)₂, assisting the formation of pores. Extended duration of calcination results in the enlarging of pores.

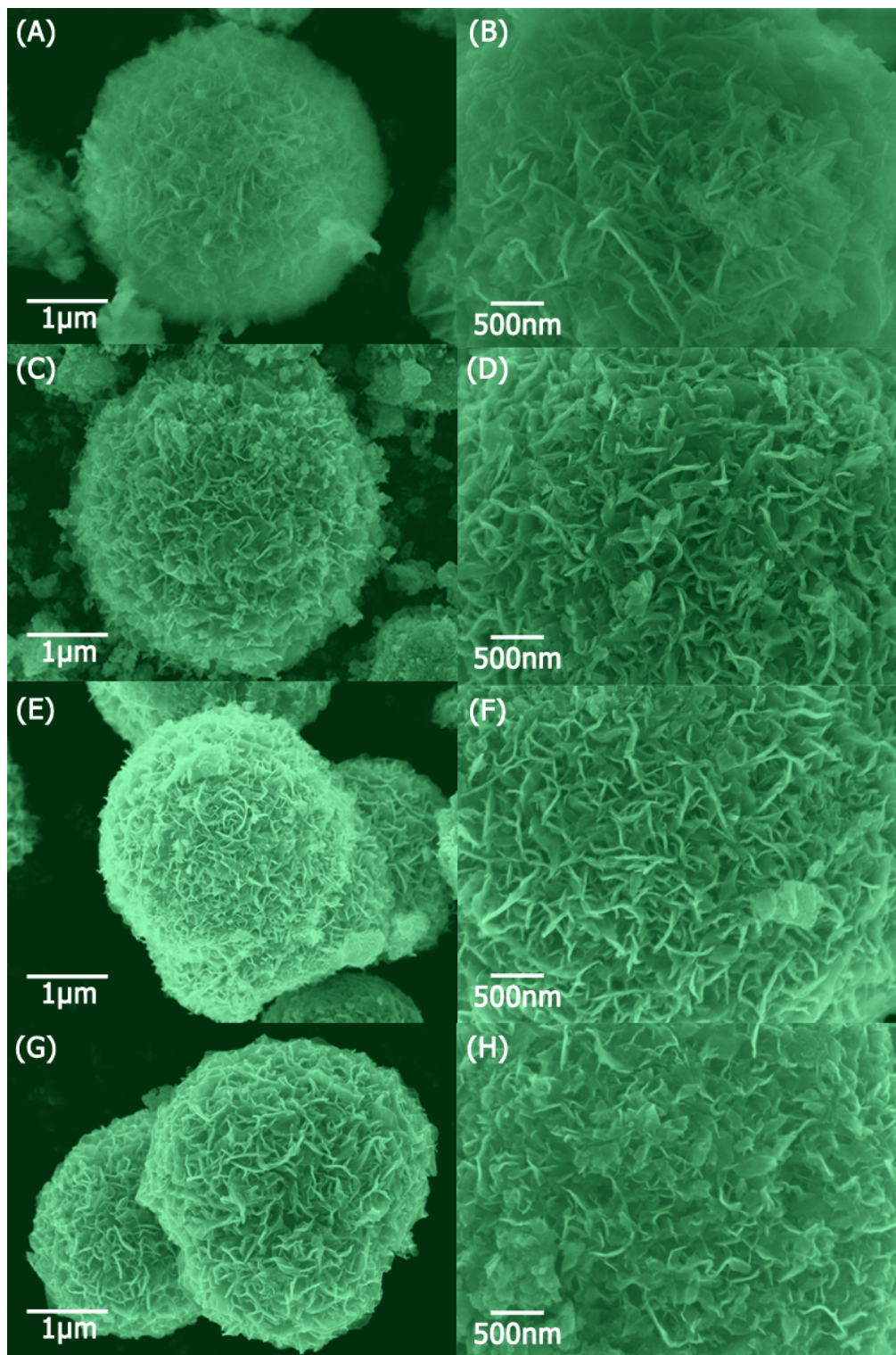


Figure 24: SEM images of (A, B) NiO-0min, (C, D) NiO-40min, (E, F) NiO-2hr, and (G, H) NiO-4hr [107]. © Elsevier

To further investigate the surface properties of the samples, the BET analysis was performed. The nitrogen adsorption-desorption isotherms are presented in **Figure 25A**. All four samples exhibit a type IV isotherm, indicating the existence of mesopores and macropores within the materials [102, 106]. Their average pore diameters range between 7 to 12 nm (**Figure 25 B**). NiO-40min was shown to have the maximum BET surface area ($169 \text{ m}^2/\text{g}$). **Table 3** summarizes the surface area and the average pore diameter for the samples.

Table 3: BET surface area and average pore diameter of NiO-0min, NiO-40min, NiO-2hr, and NiO-4hr [107].
© Elsevier

	NiO-0min	NiO-40min	NiO-2hr	NiO-4hr
BET surface area (m^2/g)	116	169	154	141
Average pore diameter (nm)	12.75	12.26	6.94	8.66

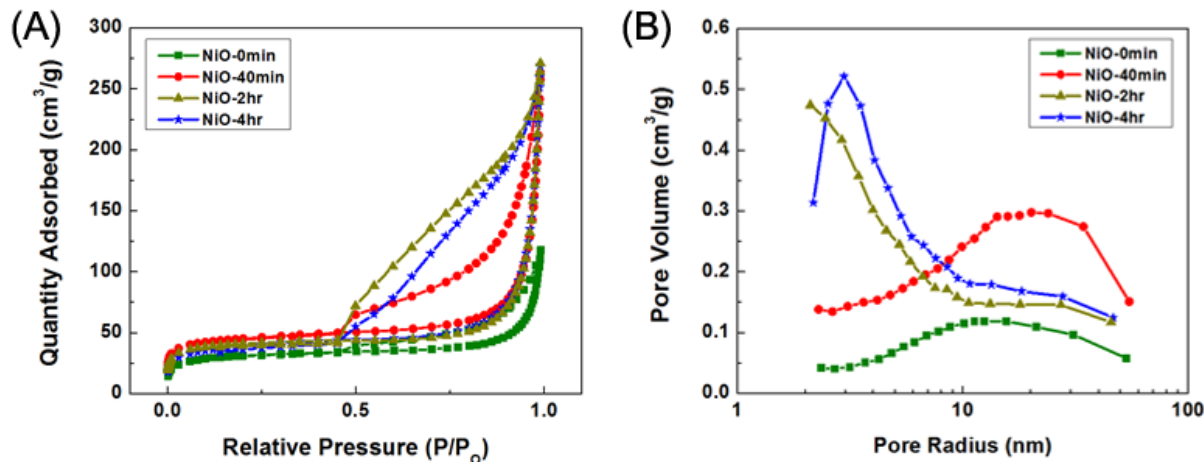


Figure 25: (A) Nitrogen adsorption-desorption isotherms of NiO-0min, NiO-40min, NiO-2hr, and NiO-4hr; (B) Pore distribution of NiO-0min, NiO-40min, NiO-2hr, and NiO-4hr [107]. © Elsevier

Studies [94, 110] have discovered that the calcination conditions (e.g. time and temperature) affect the surface area of the material. Some degree of calcination is required to increase the surface area of the Ni compounds, otherwise the removal of water and the formation of pores

would not occur and result in loss of surface area [110]. This explains why uncalcined NiO-0min has the poorest surface area. Nonetheless, extended calcination can result in an increase of grain size [94], shrinking of pore networks [104], and reduction of chemically active surface area [111, 112]. The explanation is consistent with the BET surface area results. Loss in surface area is observed for samples with higher degrees of calcination. In this context, the large surface area of NiO-40min is expected to facilitate more redox reactions during the charging process. For further analysis, cyclic voltammetry (CV), galvanostatic charge-discharge (GCD), and electrical impedance spectroscopy (EIS) were carried out on these four samples.

3.3.3 *Electrochemical Analysis*

The capacitive performance of the NiO-0min, NiO-40min, NiO-2hr, and NiO-4hr were investigated through CV analysis. The CV measurements on all four samples were performed at scan rates of 0.005, 0.01, 0.05, and 0.1 V/s using the potential window of 0.45 V (0 V to 0.45 V vs SCE). Only the lowest and the highest scan rate CV measurements are included in the **Figure 26A** and **26B**. From the CV curves, a pair of redox peaks is clearly visible for all samples, indicating the pseudocapacitive mechanism within all of the materials. However, the magnitudes of the peaks differ greatly, whereby NiO-0min has the smallest peak and NiO-40min has the largest peak. The peaks contribute to the area under the CV curves and according to **Equation 9**, the area of the curves is directly proportional to the specific capacitance.

$$C_s = \frac{\int idV}{2(m)(V_R)(V_s)} \quad \text{Equation 9}$$

Where C_s is the specific capacitance, $\int idV$ is the area of the CV curves within the assigned potential range, m is the loading mass of the active material, V_R is the potential window, and V_s is the scan rate. Applying the equation above, the specific capacitance of the samples were calculated and summarized in **Table 4**.

Table 4: Specific capacitance value of NiO-0min, NiO-40min, NiO-2hr, and NiO-4hr at scan rate of 0.005 V/s and 0.1 V/s [107]. © Elsevier

Scan Rate (V/s)	NiO-0min (F/g)	NiO-40min (F/g)	NiO-2hr (F/g)	NiO-4hr (F/g)
0.005	54	615	538	388
0.1	49	259	132	244

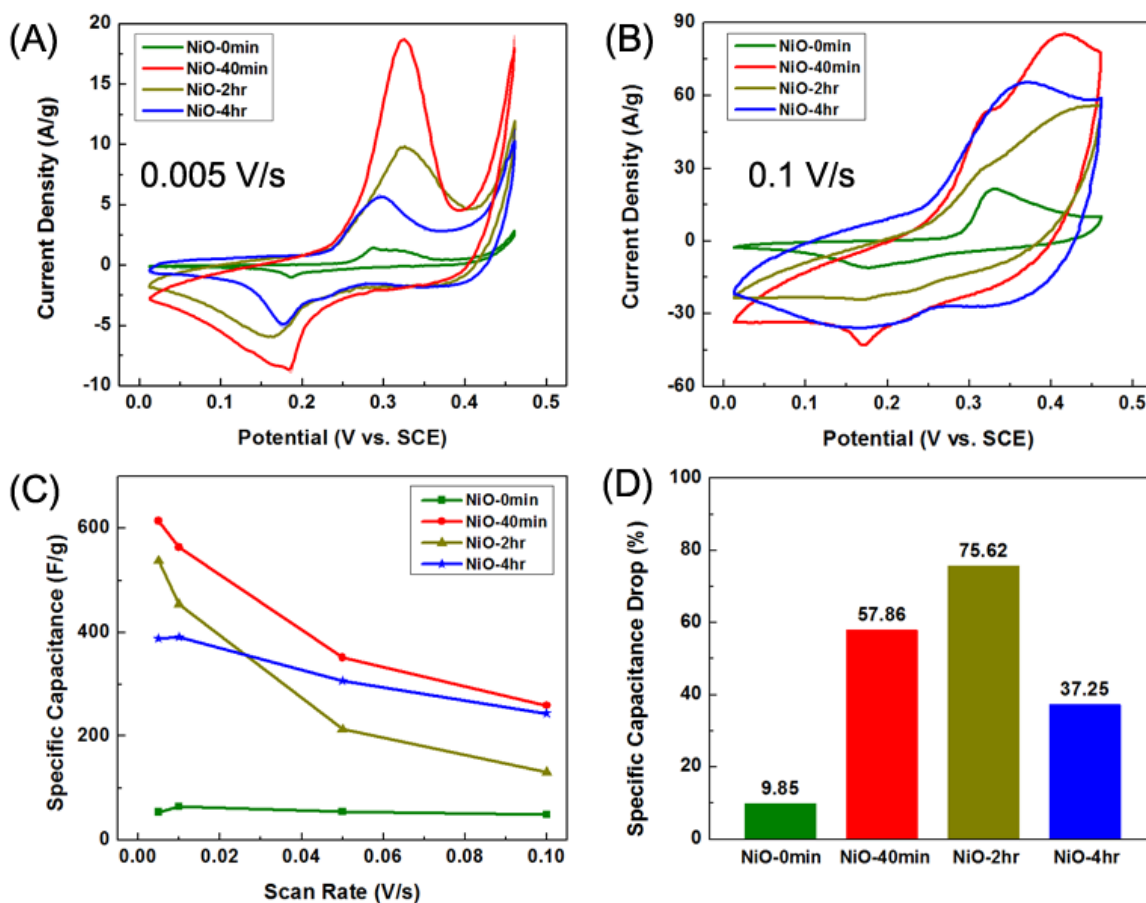


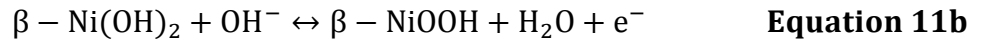
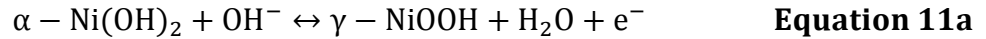
Figure 26: Cyclic voltammograms of NiO-0min, NiO-40min, NiO-2hr, and NiO-4hr at (A) 0.005V/s and (B) 0.1V/s; (C) Comparison of scan rate dependent specific capacitance of NiO-0min, NiO-40min, NiO-2hr, and NiO-4hr; and (D) Specific capacitance percentage drop of NiO-0min, NiO-40min, NiO-2hr, and NiO-4hr from scan rate at 0.005 V/s to 0.1 V/s [107]. © Elsevier

NiO-40min and NiO-2hr have higher specific capacitances than NiO-0min and NiO-4hr at 0.005 V/s, meaning the NiO/ α -Ni(OH)₂ hybrid composites (NiO-40min and NiO-2hr) exhibit superior capacitive performance than materials containing pure nickel compound (NiO-0min and NiO-4hr). A possible explanation for this result is the difference of electron transfer during the faradaic reactions of NiO and α -Ni(OH)₂. At specific applied potential, both α -Ni(OH)₂ and NiO will undergo redox reactions in KOH electrolyte, either charging or discharging electrons from the material. However, the number of electrons transferred per

nickel atom varies with the different nickel phases. For the redox reaction of NiO (**Equation 10**), nickel atoms' valence state changes from 2⁺ (NiO) to 3⁺ (NiOOH) yielding a transfer of a single electron [112, 113].



However, the number of electrons transferred for the reaction between α -Ni(OH)₂ and NiOOH is greater than one. Generally, Ni(OH)₂ is classified into two phases: α -Ni(OH)₂ and β -Ni(OH)₂. Both Ni(OH)₂ phases convert into NiOOH when they are charged in the presence of OH⁻ ions; however, different NiOOH phases are formed depending on the phases of Ni(OH)₂ as shown below [114].



One advantage of the α - γ cycle over the β - β cycle is that it can reversibly charge/discharge without inducing mechanical deformation [115]. Moreover, the α - γ cycle exchanges more electrons than the β - β cycle because the valence of the Ni atoms on γ -NiOOH is about 0.5 ~ 0.7 higher than the valence of the Ni atom on β -NiOOH [114-117]. This extra 0.5~0.7 valence charge on Ni atoms of γ -NiOOH allows the α - γ cycle to charge and discharge more electrons per redox reactions which ultimately increases the capacitive performance. As a result, NiO-40min and NiO-2hr, both consisting of the α -Ni(OH)₂ phase in the composites, show distinctive specific capacitance value at all scan rate. Additionally, the surface area could also contribute to the difference of the capacitance. NiO-40min has the highest specific capacitance at all scan rates partially could results from its largest surface area as displayed in **Table 3**.

However, NiO-40min along with NiO-2hr and NiO-4hr, experienced a significant drop in performance at higher scan rate (**Figure 26C**). Quantitatively, **Figure 26D** illustrates between 37 ~ 75% capacitance drop for the three samples when comparing the specific capacitance at scan rates of 0.005 V/s and 0.1 V/s. This is mainly caused by the low conductivity of α -Ni(OH)₂ and NiO. Both nickel compounds lack conductivity, leading to sluggish electron transfer rate of the redox reactions and reduction of capacitive performance at high scan rates [118]. For NiO-0min, no significant reduction of performance was observed as the sample already displays low performance at slow scan rate from the combined effects of poor conductivity and small surface area. The conductivity of the four samples will be thoroughly discussed in a proceeding chapter with EIS analysis. Overall, NiO-40min outperformed all of the samples, achieving the highest specific capacitance at all scan rates.

The above observations are also seen for GCD analysis. **Figure 27A** and **27B** show the GCD curves collected from the applied current density of 2 A/g and 10 A/g. A non-linear discharge curve is visible for all of the samples verifying the occurrence of faradaic reaction on the surface of the materials. The specific capacitance can be calculated from the GCD curves using the equation below.

$$C_s = \frac{(\Delta t)(I_A)}{(\Delta V)} \quad \text{Equation 12}$$

where C_s is the specific capacitance, Δt is the discharging time of the applied potential difference, I_A is the applied current density, and ΔV is the applied potential difference.

Figure 27A shows the extended discharge time is required for NiO-40min which

corresponds to the highest specific capacitance of 707 F/g; on the contrary, NiO-0min shows a very quick discharge with the value of 74 F/g. **Table 5** lists the specific capacitance values for the samples.

Table 5: Specific capacitance value of NiO-0min, NiO-40min, NiO-2hr, and NiO-4hr at current density of 2 A/g and 10 A/g [107]. © Elsevier

Current Density (A/g)	NiO-0min (F/g)	NiO-40min (F/g)	NiO-2hr (F/g)	NiO-4hr (F/g)
2	74	707	558	393
10	51	474	338	351

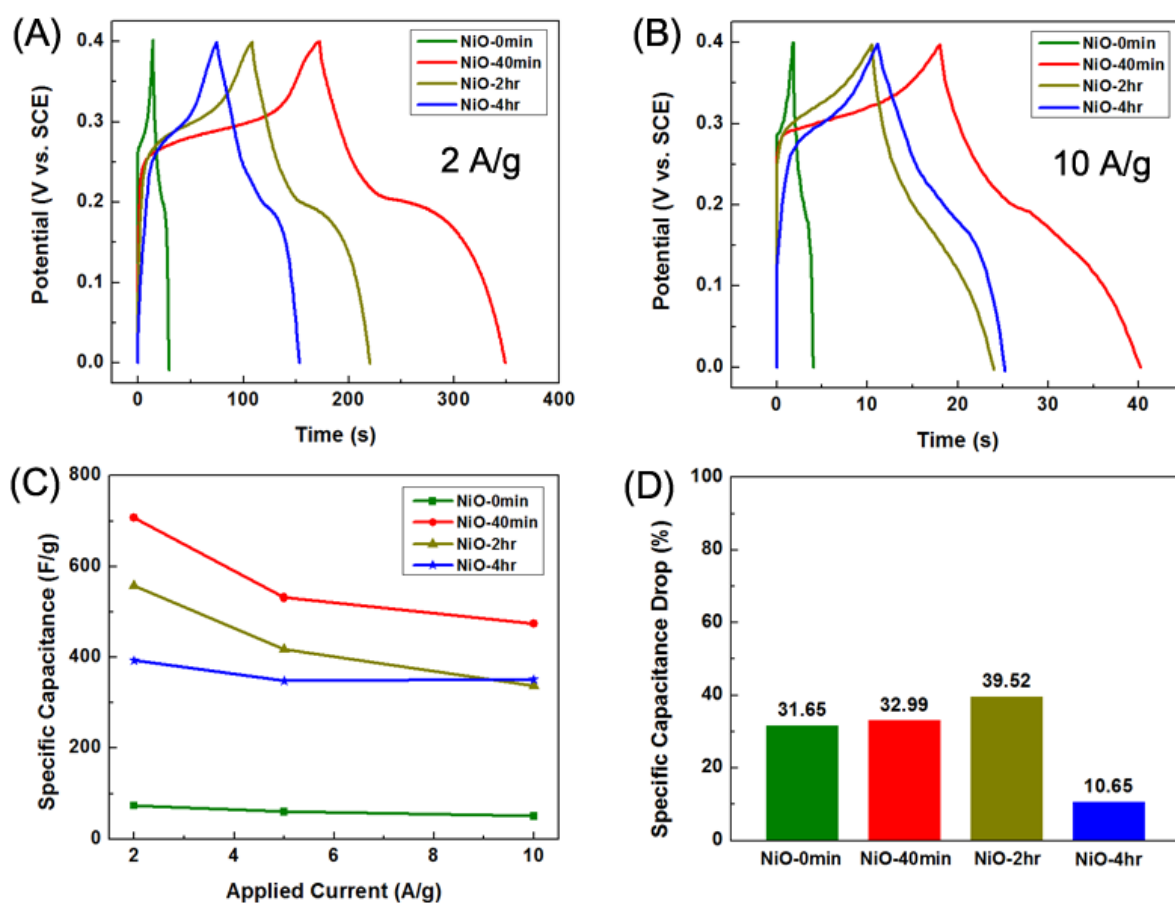


Figure 27: Galvanostatic charge-discharge curve of NiO-0min, NiO-40min, NiO-2hr, and NiO-4hr at (A) 2 A/g and (B) 10 A/g; (C) Comparison of applied current dependent specific capacitance of NiO-0min, NiO-40min,

NiO-2hr, and NiO-4hr; and (D) Specific capacitance percentage drop of NiO-0min, NiO-40min, NiO-2hr, and NiO-4hr from applied current at 2 A/g to 10 A/g [107]. © Elsevier

The trend is identical for both CV and GCD results. The NiO/ α -Ni(OH)₂ composites show a higher capacitive value than the pure NiO or α -Ni(OH)₂. However, the specific capacitance value dropped significantly for the hybrid composites when the applied current density increased (**Figure 27C**). The poor conductivity of the hybrid composite is again evident in these results. NiO-40min lost 33% of its capacitive performance when applied current was increased by 5 times, but it still retains the highest capacitance at 10 A/g and at any current densities (**Figure 27D**). Thus, the overall capacitance trend from CV and GCD is consistent. Impedance analysis was performed for all samples to determine their overall resistance. The samples were subjected to AC impedance with a frequency range of 0.1 Hz to 100 kHz at a potential amplitude of 0.32 V versus reference potential. **Figure 28A** shows the Nyquist plot (imaginary part (Z_{im}) versus real part (Z_{re})) of the four samples. The plot was fitted with Zsimpwin computer software to generate an equivalent circuit and quantify several circuit parameters for further analysis (**Figure 28B**) [105, 119]. Many circuit parameters are included for accurate fitting of the impedance data. The Nyquist plot can be divided into three sections: high, medium, and low frequency. The system's electrical series resistance (R_{esr}) can be determined from the high frequency region, shown in the inset of the **Figure 28A**. The intercept at the real part (Z_{re}) is the R_{esr} which is comprised of electrolyte resistance [120], and contact resistance between the interface of active material and current collectors [121]. The R_{esr} of the samples are similar, ranging between 0.6 to 0.73 $\Omega \cdot \text{cm}^2$, validating the consistent testing systems (*e.g.* three-point probe setup and electrolyte concentrations). Semicircle impedance arcs are seen for NiO-40min, NiO-2hr, and NiO-4hr at the medium

frequency range. The impedance arcs could be used to approximate the diameters of semicircles which represent the combination of the ionic charge transfer resistance (R_{it}) and the electron charge transfer resistance (R_{et}) within NiO and α -Ni(OH)₂ along with the faradaic redox process [119, 122]. Shorter diameter of the semicircles indicate that the ionic and electrical resistance of the material is small [123]. From fitting the impedance data with the equivalent circuits, the combined values of R_{it} and R_{et} are shown in **Table 6** below.

Table 6: Fitted R_{esr} and combination of R_{it} and R_{et} of NiO-0min, NiO-40min, NiO-2hr, and NiO-4hr [107]. © Elsevier

	NiO-0min	NiO-40min	NiO-2hr	NiO-4hr
R_{esr} ($\Omega \cdot \text{cm}^2$)	0.605	0.707	0.731	0.697
$R_{it} + R_{et}$ ($\Omega \cdot \text{cm}^2$)	655.7	5.2	3.2	1.7

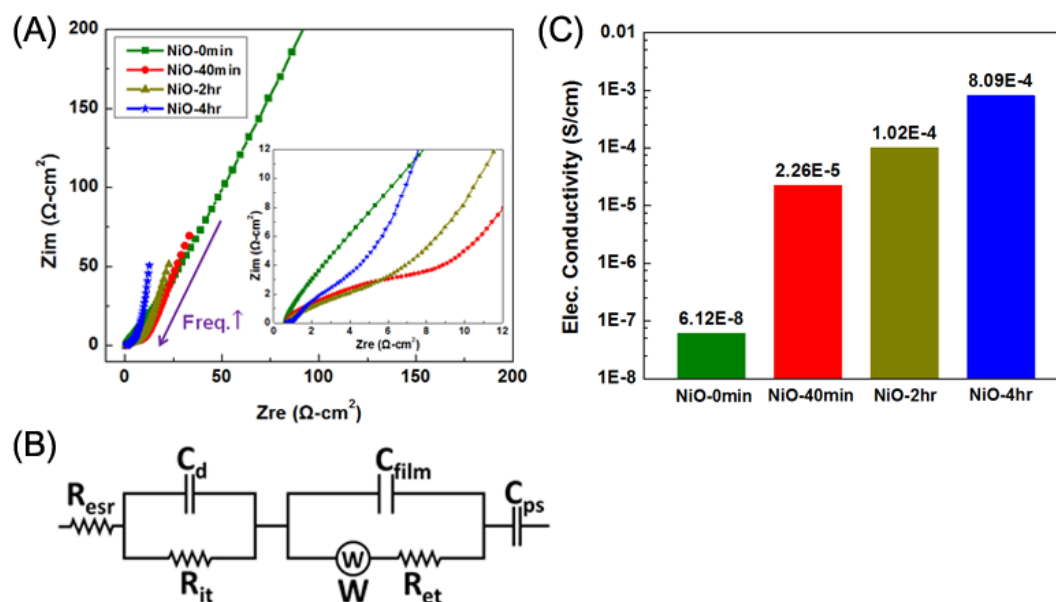


Figure 28: (A) Nyquist impedance spectra of NiO-0min, NiO-40min, NiO-2hr, and NiO-4hr; the inset shows impedance at high frequency region; (B) Equivalent circuit fitted for the impedance spectra where R_{esr} is the electrical series resistance, C_d is the double layer capacitance, R_{it} is the ionic charge transfer resistance, C_{film} is

the film capacitance, W is the Warburg diffusion resistance, R_{et} is the electron charge transfer resistance, and C_{ps} is the pseudocapacitance; (C) Electrical conductivity of NiO-0min, NiO-40min, NiO-2hr, and NiO-4hr in logarithmic scale from four-point probe technique [107]. © Elsevier

NiO-4hr has the lowest ionic/electron charge transfer resistance because it is fully composed of NiO which is more conductive than α -Ni(OH)₂ [124]. Warburg impedance occurs in the low frequency region, represented by a sloped line in the Nyquist plot and labeled as W in the equivalent circuit. Warburg impedance describes the diffusion limited system where anions and cations are required to travel through the ionic pathway in the materials to form faradaic reaction [119, 125]. Steep impedance line indicates the sample follows an ideal capacitor as more capacitance results from pseudocapacitive redox reaction at low frequency [104, 124]. A shorter Warburg line implies a lower diffusion resistance in the material and a shorter ionic path for the storage of hydroxide ions which ultimately provides better capacitive performance [123, 124]. According to **Figure 28A**, NiO-4hr has the steepest and the shortest impedance line, showing superior diffusion of hydroxide ions over the other samples. Furthermore, similar trend from the impedance result is observed with the electrical conductivity measurement of the four samples (**Figure 28C**). NiO-0min exhibits the poorest conductivity; however, the conductivity drastically improves by more than three orders when poorly conductive α -Ni(OH)₂ are calcined and converted to semi-conducting NiO. Significant increases in conductivity are evident as the duration of calcination extends because more α -Ni(OH)₂ are converted into NiO. As a result, NiO-4hr is the most conductive material. But due to the relatively low surface area, its performance is slightly lower than that of NiO-40min. Therefore, in order to retain the exceptional specific capacitance for NiO compound at high testing conditions, addition of conductive support is recommended.

3.4 The Effects of Carbon

The study has shown that both NiO and α -Ni(OH)₂ have poor electrical conductivity, resulting in reduced capacitive performance and slow electron transport at high electrical rates, limiting its practical application [118]. To resolve the issue, researchers commonly incorporate carbon black into the nickel compounds to maximize the capacitance of the pseudocapacitive material [126]. Although, an investigation to find the most suitable carbon support other than carbon black for NiO/ α -Ni(OH)₂ is recommended.

We studied the impact of different carbon supports, including carbon black, carbon nanotubes, and reduced graphene oxide (rGO), on the hybrid composite and to our surprise, the study revealed that the nickel hybrid composite supported with single-walled carbon nanotubes (SWCNTs) outperformed rGO and exhibited the best performance. The composite with 20 wt% addition of SWCNTs demonstrated a capacitance of 828 F/g at current discharge of 2 A/g and 810 F/g at a high current discharge of 10 A/g, showing only 2% drop. Our results clearly show the addition of the carbon supports dramatically enhances the capacitive performance and capacitance retention of the nickel hybrid composite. The hybrid nickel oxide/hydroxide with the support of different carbon supports, especially SWCNTs, is a good candidate for development of electrodes for high performance ECs.

3.5 Experimental Procedure

3.5.1 *Synthesis of Reduced Graphene Oxide (rGO)*

Before synthesizing rGO, graphitic oxide (GO) was prepared from the graphite powder following the modified Hummer's method [127]. To obtain rGO, 400 mg of prepared GO was sonicated in 40 mL of DDI water until uniformly dispersed. Then 5% Na_2CO_3 was added into the solution to adjust the pH to 10 and then 3 g NaBH_4 dissolved in 50 mL DDI water was added. The solution was stirred at 80°C for 2 days. The reduction process was repeated once more to remove residual oxygen groups. The finished solution was washed with DDI and ethanol and freeze-dried.

3.5.2 *Preparation of Nickel Hybrid Composite with Carbon Supports*

Four different carbon supports were tested: Ketjenblack (KB), reduced graphene oxide (rGO), multi-walled carbon nanotubes (MWCNT), and single-walled carbon nanotubes (SWCNT). The carbon supported nickel composites were prepared by thorough mixing of 80 wt% of NiO-40min and 20 wt% of carbon supports with a mortar and pestle. Out of the four nickel samples, NiO-40min was chosen for its excellent capacitive performance. After mixing, the flower morphology was retained and the samples were denoted accordingly to the type of carbons used, particularly: NiO-KB, NiO-rGO, NiO-MWCNT, and NiO-SWCNT.

3.6 Results and Discussions

In summary, NiO/ α -Ni(OH)₂ composites show promising specific capacitance at low scan rate and applied current density. Specifically, the NiO-40min demonstrated excellent capacitive performance among all samples. Thus, the addition of conductive supports to NiO-40min, such as carbon supports, was further investigated in order to capitalize on the excellent capacitive performance and large surface areas at high testing frequencies. Carbon supports are generally known to improve the conductivity of an electrode [5]. Depending on morphologies and material properties, carbons' contributions could vary. Thus, electrochemical testing is performed to measure the capacitive performance of the carbon supported NiO; the result was also compared with bare NiO-40min. For clarification, NiO in the name of the samples refers to NiO-40min. **Figure 29A** shows the CV curves of NiO-40min and carbon mixed NiO-40min at a scan rate of 0.005 V/s. All samples show the distinctive redox peak, indicating the existence of faradaic reaction of NiO and α -Ni(OH)₂. Comparing the magnitudes of the peaks, it reveals that all carbon supported NiO-40min show better capacitance than NiO-40min, ranging between 640 F/g to 760 F/g at a scan rate of 0.005 V/s with the maximum capacitance observed for NiO/SWCNT. NiO-40min without carbon supports shows lowest capacitance value of 614 F/g. More distinctive difference in performance is observed at higher scan rate. In **Figure 29B**, the faradaic peaks of NiO-40min without carbon support diminish due to the conductivity issue discussed earlier in this paper. Therefore, a steeper loss in specific capacitance for NiO-40min is visible than the other carbon supported samples at a faster scan rate (**Figure 29C**). NiO-40min lost 58% of its

performance when comparing the capacitance measured at 0.005 V/s and 0.1 V/s (**Figure 29D**). Meanwhile, NiO/MWCNT and NiO/SWCNT show remarkable retention of performance with only 17% and 16% loss, respectively. NiO/rGO shows a higher loss of 28%. The difference in performance of the carbons will be discussed later in the study. Overall, the CV results validate that adding carbons to NiO/ α -Ni(OH)₂ composites significantly improves the capacitance.

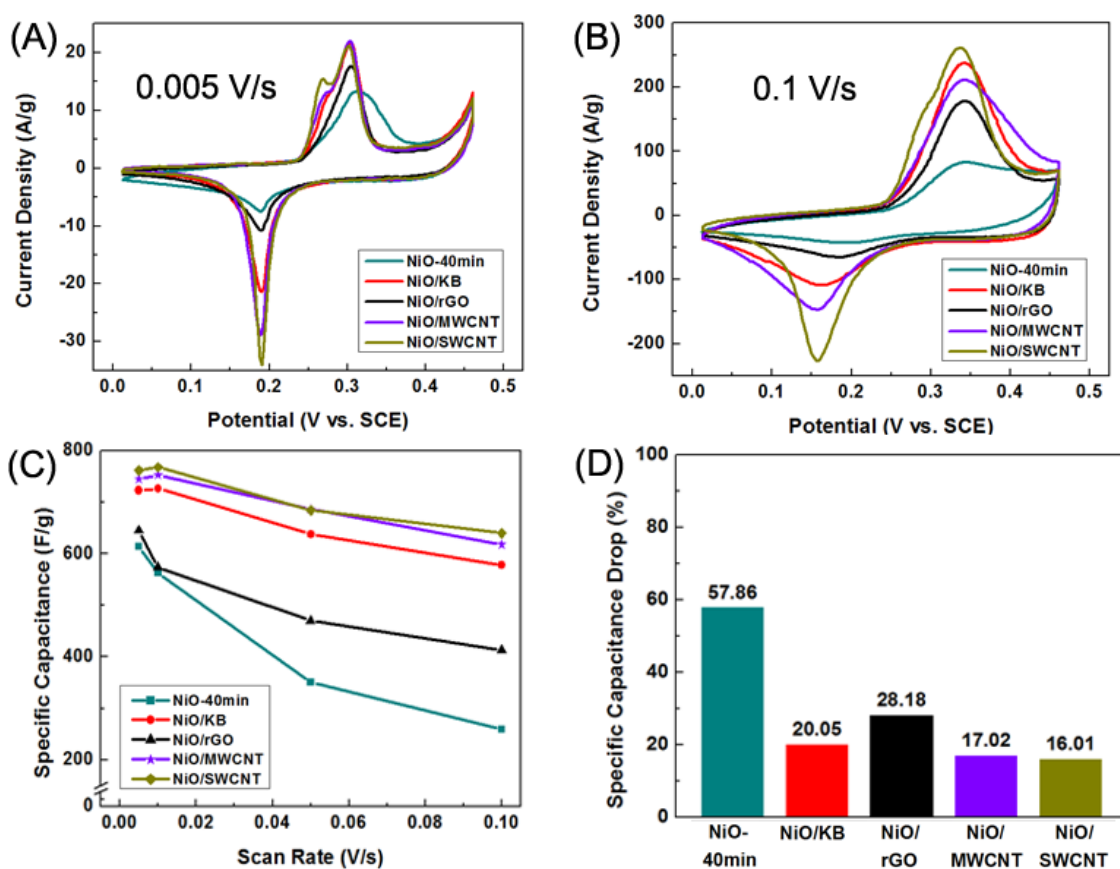


Figure 29: Cyclic voltammograms of NiO-40min, NiO/KB, NiO/rGO, NiO/MWCNT, and NiO/SWCNT at (A) 0.005 V/s and (B) 0.1 V/s; (C) Comparison of scan rate dependent specific capacitance of NiO-40min, NiO/KB, NiO/rGO, NiO/MWCNT, and NiO/SWCNT; and (D) Specific capacitance percentage drop of NiO-40min, NiO/KB, NiO/rGO, NiO/MWCNT, and NiO/SWCNT from scan rate at 0.005 V/s to 0.1 V/s [107]. © Elsevier

A similar trend is seen with the galvanostatic charge/discharge (GCD) curves in **Figure 30A** and **30B**. The specific capacitances calculated from GCD analysis are listed in **Table 7** below.

Table 7: Specific capacitance value of NiO-40min, NiO/KB, NiO/rGO, NiO/MWCNT, and NiO/SWCNT at current density of 2 A/g and 10 A/g [107]. © Elsevier

Current Density (A/g)	NiO-40min (F/g)	NiO/KB (F/g)	NiO/rGO (F/g)	NiO/MWCNT (F/g)	NiO/SWCNT (F/g)
2	707	769	628	799	828
10	474	575	575	780	810

However, NiO-40min suffers continuous capacitance loss as current density increases, while the carbon supported NiO samples performed consistently even at a high current density of 10 A/g (**Figure 30C**). For instance, **Figure 30D** illustrates the excellent performance retention of NiO/MWCNT and NiO/SWCNT when comparing the specific capacitance measured at 2 A/g and 10 A/g. Meanwhile, NiO/rGO showed relatively low performance in both CV and GCD analysis. When the investigation of different carbon supports was first commenced, rGO was presumed to be the best carbon support due to its unique 2D structure as 2D nanomaterials generally give low contact resistance. But surprisingly, carbon nanotubes were better in performance. This can be explained by the poor conductivity of the rGO resulting from the functionalities and the restacking of rGO sheets. The conductivity of chemically reduced rGO is reported to be between 0.5 to 40 S/cm [128, 129], which is significantly lower than SWCNTs' conductivity (250 to 400 S/cm) [130]. Thus, SWCNTs provide an easier electrical conductive pathway for the transport of electrons than rGO. In addition, several studies have found that stacking of rGO sheets inhibits the utilization of the surface area [131], and causes ionic diffusion limitation [132], and electron transfer

resistance [132]. Together, these effects can decrease the capacitive performance of NiO/rGO. From both CV and GCD curves, NiO/SWCNT and NiO/MWCNT exhibit higher specific capacitance than NiO/KB because both CNTs have higher aspect ratio than KB which is ideal for wiring conductive pathway for electrons and electrolyte ions [133]. In **Figure 30C**, NiO/SWCNT displays an average of 50 F/g more than NiO/MWCNT for all current densities since the specific capacitance of SWCNTs are generally reported around 180 F/g whereas MWCNTs are known to provide 102 F/g [37, 134]. **Table 7** summarized the capacitances of different materials at current density of 2 A/g and 10 A/g, respectively.

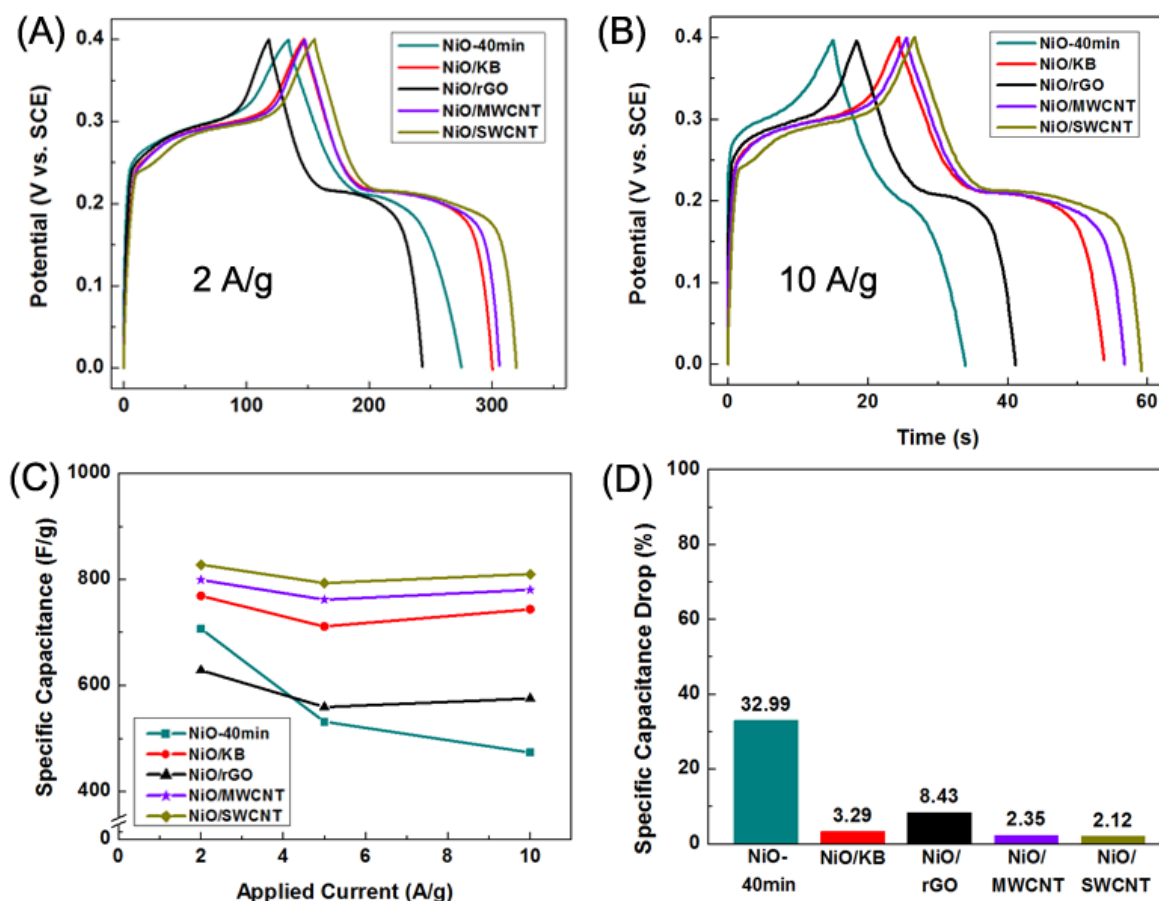


Figure 30: Galvanostatic charge-discharge curve of NiO-40min, NiO/KB, NiO/rGO, NiO/MWCNT, and NiO/SWCNT at (A) 2 A/g and (B) 10 A/g; (C) Comparison of applied current dependent specific capacitance of NiO-40min, NiO/KB, NiO/rGO, NiO/MWCNT, and NiO/SWCNT; and (D) Specific capacitance percentage

drop of NiO-40min, NiO/KB, NiO/rGO, NiO/MWCNT, and NiO/SWCNT from applied current at 2 A/g to 10 A/g [107]. © Elsevier

Superior conductivity of SWCNTs is more evident from the EIS impedance data, shown in **Figure 31A**. The inset of **Figure 31A** shows that NiO/SWCNT has the smallest semicircle diameter, implying that it has the lowest ionic resistance out of the entire sample set [123]. Overall, all carbon supported NiO-40min have smaller semi-circle and shorter Warburg impedance than NiO-40min which verifies that the addition of carbon materials improved the conductivity and the capacitance performance of the NiO/ α -Ni(OH)₂ composite.

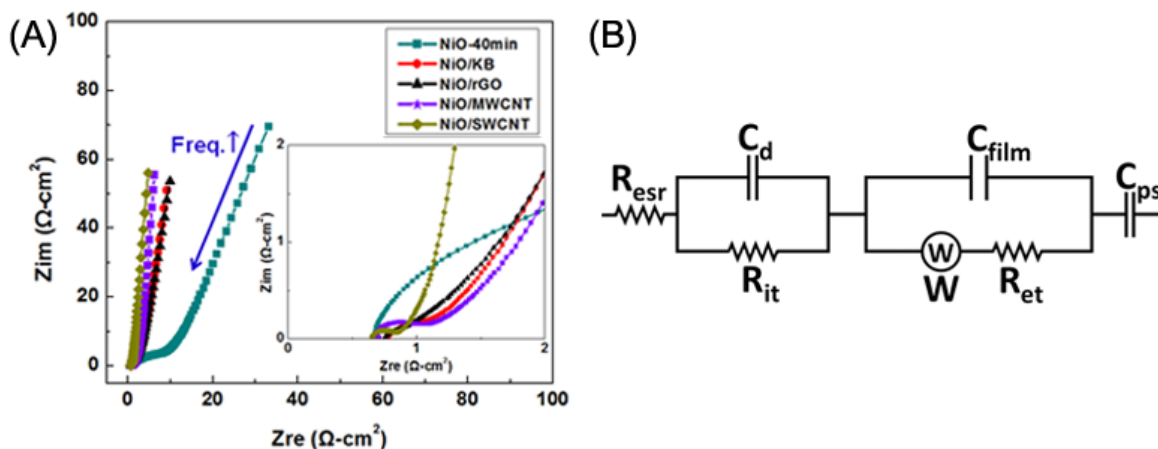


Figure 31: (A) Nyquist impedance spectra of NiO-40min, NiO/KB, NiO/rGO, NiO/MWCNT, and NiO/SWCNT; the inset shows impedance at high frequency region; (B) Equivalent circuit fitted for the impedance spectra where R_{esr} is the electrical series resistance, C_d is the double layer capacitance, R_{it} is the ionic charge transfer resistance, C_{film} is the film capacitance, W is the Warburg diffusion resistance, R_{et} is the electron charge transfer resistance, and C_{ps} is the pseudocapacitance [107]. © Elsevier

Figure 32A illustrates the cycle stability of the NiO/ α -Ni(OH)₂ hybrid composite and its carbon supported samples. An increase in capacitance retention is observed after 50 cycles for all samples. This is believed to be caused by the activation of the material through repetitive charging and discharging. During the initial cycles, more and more electrochemically active sites are beginning to be utilized and small pores are being fully

accessed by the electrolyte; hence increasing the capacitance. NiO-40min demonstrates consistent cycle stability without significant capacitance fade from its initial value after 800 cycles. Nonetheless, decay in capacitance retention is apparent for carbon supported samples. This is perhaps attributed to the breaking off of the carbon additives from the NiO/ α -Ni(OH)₂ composite after repetitive cycling. Since the carbon additives and the nickel compound were physically mixed using a mortar and pestle, their bond may have been physically severed under the intense charge/discharge process. To reduce the capacitance loss at longer cycle, future research aims to perform in-situ growth of NiO/ α -Ni(OH)₂ and carbon supports to form strong chemical linkage.

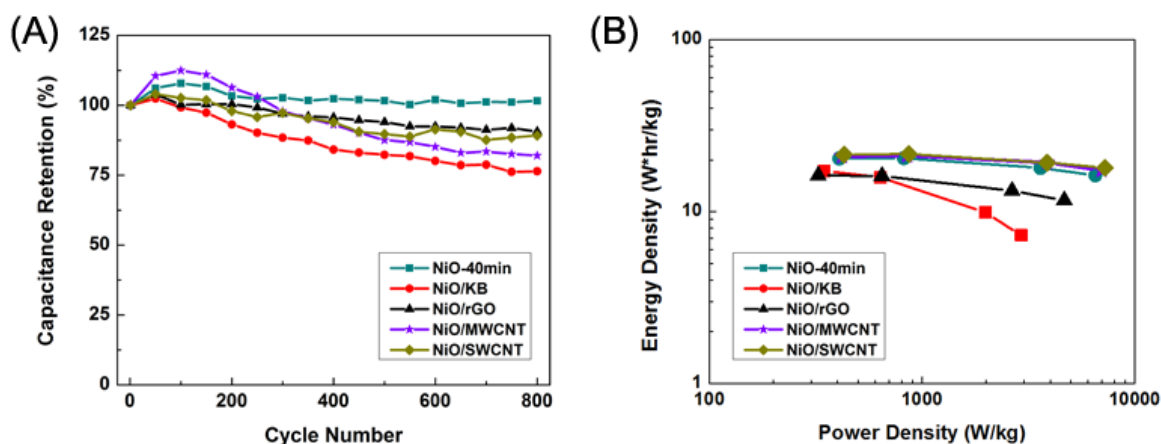


Figure 32: (A) Cycle stability of NiO-40min, NiO/KB, NiO/rGO, NiO/MWCNT, and NiO/SWCNT at a current density of 10 A/g (B) Ragone plot of NiO-40min, NiO/KB, NiO/rGO, NiO/MWCNT, and NiO/SWCNT [107]. © Elsevier

Further analysis of energy and power performance of the material is carried out by plotting the Ragone plot (**Figure 32B**). The energy density (E.D.) was derived from the CV measurements at 0.005 V/s, 0.01 V/s, 0.05 V/s, and 0.1 V/s, using **Equation 6**. From **Equation 8**, the average power density ($P.D_{Avg}$) can be calculated. The Ragone plot illustrates that the carbon supported NiO-40min provided high power density without losing

significant energy density whereas NiO-40min without carbon additives lost energy density at higher power density due to the lack of conductivity. This considerable improvement suggests addition of carbon support is necessary to capitalize the excellent capacitive performance of NiO-40min. The maximum energy density of 21 Wh/kg and the maximum power density of 7220 W/kg were obtained from NiO-SWCNT. Thus, NiO-40min with SWCNT support is more suitable for EC applications.

3.7 Summary

Self-assembled flower-like α -Ni(OH)₂ were synthesized by a facile solvothermal method at 110°C for 15 hours. The composition of the NiO/ α -Ni(OH)₂ hybrid composite was formed by tuning the calcination duration with the crystal phases present identified by XRD. The SEM images verified the flower morphology was developed during the synthesis and the structure of the nickel composite was maintained throughout the heat treatment. Nitrogen adsorption/desorption isotherm indicates the existence of mesopores and macropores in the material. From the electrochemical analysis, the NiO/ α -Ni(OH)₂ composite has superior pseudocapacitive performance than the individual α -Ni(OH)₂ and NiO, but poor electronic conductivity hindered its capacitance retention at high current density. The effects of different carbon supports on the hybrid composite have been investigated and CNTs, especially SWCNTs, are concluded to provide the highest performance with a specific capacitance of 810 F/g at 10 A/g, possibly attributed from outstanding electrical conductivity of SWCNTs. Moreover, this carbon supported hybrid composite exhibits an impressive specific power density of 7200 W/kg and a steady energy density of 21 Wh/kg. The hybrid

nickel oxide/hydroxide with the support of different carbon supports, especially SWCNTs, is a good candidate for development of next generation ECs.

Chapter 4: Perspectives of Future Work

In summary, two sets of experiments were undertaken to develop nickel hydroxide/oxide hybrid materials for EC applications and to select the best carbon support through analysis of their effects on capacitive performance. The first set of experiments focused on synthesizing the nickel hybrid structure and confirming the atomic structure, morphology, and capacitive performance through physical and electrochemical characterization. In conclusion, NiO-40min, a composite of α -Ni(OH)₂ and NiO, exhibited the highest specific capacitance, but it suffered a drastic loss in performance at high testing conditions. Therefore, as an enhancement to the nickel hybrid material, different types of carbon were added as supports. Between activated carbon, carbon nanotubes, and graphene, single-walled carbon nanotubes demonstrated the best results when combined with the nickel hydroxide/oxide composite. Based on the findings of the study, some future directions for ECs concerning pseudocapacitive materials can be suggested:

1. Synthesis of hybrid structures for other transition metals (*e.g.* cobalt oxide, copper oxide) by tailoring the calcination temperature and duration.
2. Verification of the conclusion concerning NiO-rGO through use of commercially available reduced graphene oxide.
3. Chemically bonding the nickel hydroxide/oxide on the carbon supports rather than physically mixing them.
4. Synthesis of a full asymmetric electrochemical capacitor with a carbon supported nickel hydroxide/oxide as the cathode and reduced graphene oxide as the anode.

References

[1] A. Yu, V. Chabot, J. Zhang, Electrochemical Supercapacitors for Energy Storage and Delivery, Taylor & Francis Group, LLC, Boca Raton, Florida, 2013.

[2] H.I. Becker, Low Voltage Electrolytic Capacitor, in: U.S.P. Office (Ed.), United States of America, 1957.

[3] D.L. Boos, Electrolytic Capacitor having Carbon Paste Electrodes, in: U.S.P. Office (Ed.), The Standard Oil Company, Cleveland, Ohio, US, 1970.

[4] M. Endo, T. Takeda, Y.J. Kim, K. Koshiba, K. Ishii, High Power Electric Double Layer Capacitor (ELDC's); from Operating Principle to Pore Size Control in Advanced Activated Carbons, Carbon Science, 1 (2001) 117-128.

[5] A.G. Pandolfo, A.F. Hollenkamp, Carbon properties and their role in supercapacitors, J Power Sources, 157 (2006) 11-27.

[6] L.L. Zhang, X.S. Zhao, Carbon-based materials as supercapacitor electrodes, Chem Soc Rev, 38 (2009) 2520-2531.

[7] A. Yu, A. Davies, Z. Chen, Electrochemical Supercapacitors, in: R.S. Liu, Z. Lei, X. Sun, H. Liu, J. Zhang (Eds.) *Electrochemical Technologies for Energy Storage and Conversion*, vol. 1, Wiley-VCH Verlag & Co. KGaA, Weinheim, Germany, 2012, pp. 317.

[8] P. Simon, Y. Gogotsi, Materials for electrochemical capacitors, *Nat Mater*, 7 (2008) 845-854.

[9] Y.W. Zhu, S. Murali, M.D. Stoller, K.J. Ganesh, W.W. Cai, P.J. Ferreira, A. Pirkle, R.M. Wallace, K.A. Cychoz, M. Thommes, D. Su, E.A. Stach, R.S. Ruoff, Carbon-Based Supercapacitors Produced by Activation of Graphene, *Science*, 332 (2011) 1537-1541.

[10] B.E. Conway, Transition from Supercapacitor to Battery Behavior in Electrochemical Energy-Storage, *J Electrochem Soc*, 138 (1991) 1539-1548.

[11] B.E. Conway, *Electrochemical Supercapacitors*, Plenum Publishing, New York, 1999.

[12] C.C. Hu, K.H. Chang, M.C. Lin, Y.T. Wu, Design and tailoring of the nanotubular arrayed architecture of hydrous RuO₂ for next generation supercapacitors, *Nano Lett*, 6 (2006) 2690-2695.

[13] Y.Y. Gao, S.L. Chen, D.X. Cao, G.L. Wang, J.L. Yin, Electrochemical capacitance of Co₃O₄ nanowire arrays supported on nickel foam, *J Power Sources*, 195 (2010) 1757-1760.

[14] J. Zhang, L.B. Kong, H. Li, Y.C. Luo, L. Kang, Synthesis of polypyrrole film by pulse galvanostatic method and its application as supercapacitor electrode materials, *J Mater Sci*, 45 (2010) 1947-1954.

[15] A. Malak, K. Fic, G. Lota, C. Vix-Guterl, E. Frackowiak, Hybrid materials for supercapacitor application, *J Solid State Electr*, 14 (2010) 811-816.

[16] Z.S. Wu, W.C. Ren, D.W. Wang, F. Li, B.L. Liu, H.M. Cheng, High-Energy MnO₂ Nanowire/Graphene and Graphene Asymmetric Electrochemical Capacitors, *Acs Nano*, 4 (2010) 5835-5842.

[17] Z.J. Fan, J. Yan, T. Wei, L.J. Zhi, G.Q. Ning, T.Y. Li, F. Wei, Asymmetric Supercapacitors Based on Graphene/MnO₂ and Activated Carbon Nanofiber Electrodes with High Power and Energy Density, *Adv Funct Mater*, 21 (2011) 2366-2375.

[18] M. Conner, Supercapacitor-powered screwdriver recharges in 90 seconds, in, *EDN Network*, 2007.

[19] M.L. Wald, Remote controls, without the AAA batteries, in, *The New York Times Bits*, 2013.

[20] C. Denison, This wireless bamboo speaker charges in 5 minutes and plays for 6 hours, in, *Digital Trends*, 2013.

[21] B. Andrews, Advent of ultracapacitors signals change in wind turbine capabilities, in, *Renewableenergyworld.com*, 2011.

[22] R. Hubley, Green energy used by capital's new cable car, in, SourceWire News Distribution, 2012.

[23] Railway-Gazette, Trams to harvest regenerative braking, in, Energy Harvesting Journal, 2012.

[24] H. Hondius, Supercapacitors to be tested on Paris STEEM tram, in, Railway Gazette, 2009.

[25] T. Hamilton, Next stop: ultracapacitor buses, in, MIT Technology Review, 2009.

[26] A. Ingram, Volvo develops structural supercapacitor nanobatteries for future electric cars, in, Green Car Reports, 2013.

[27] A.C. Estes, These new graphene supercapacitors could finally power an electric car, in, Gizmodo, 2013.

[28] K. Jost, D. Stenger, C.R. Perez, J.K. McDonough, K. Lian, Y. Gogotsi, G. Dion, Knitted and screen printed carbon-fiber supercapacitors for applications in wearable electronics, *Energy Environ Sci*, 6 (2013) 2698-2705.

[29] S. Powell, Clothing the body electric: fabric in modified T-shirt can store electrical charge, in, University of South Carolina, 2012.

[30] P. Harrop, Supercapacitors gain ascendancy, in, Electronics Maker, 2013.

[31] A.D. Angelis, Supercapacitors market to increase at a CAGR of 19.85% through 2016, in, Energy and Utilities, 2013.

[32] D.Y. Qu, Studies of the activated carbons used in double-layer supercapacitors, J Power Sources, 109 (2002) 403-411.

[33] E. Frackowiak, Carbon materials for supercapacitor application, Phys Chem Chem Phys, 9 (2007) 1774-1785.

[34] Z.B. Wen, Q.T. Qu, Q. Gao, X.W. Zheng, Z.H. Hu, Y.P. Wu, Y.F. Liu, X.J. Wang, An activated carbon with high capacitance from carbonization of a resorcinol-formaldehyde resin, Electrochem Commun, 11 (2009) 715-718.

[35] C.M. Niu, E.K. Sichel, R. Hoch, D. Moy, H. Tennent, High power electrochemical capacitors based on carbon nanotube electrodes, Appl Phys Lett, 70 (1997) 1480-1482.

[36] K.K.S. Lau, J. Bico, K.B.K. Teo, M. Chhowalla, G.A.J. Amaratunga, W.I. Milne, G.H. McKinley, K.K. Gleason, Superhydrophobic carbon nanotube forests, Nano Lett, 3 (2003) 1701-1705.

[37] R.H. Baughman, A.A. Zakhidov, W.A. de Heer, Carbon nanotubes - the route toward applications, Science, 297 (2002) 787-792.

- [38] L.B. Hu, J.W. Choi, Y. Yang, S. Jeong, F. La Mantia, L.F. Cui, Y. Cui, Highly conductive paper for energy-storage devices, *P Natl Acad Sci USA*, 106 (2009) 21490-21494.
- [39] R.G. Ding, G.Q. Lu, Z.F. Yan, M.A. Wilson, Recent advances in the preparation and utilization of carbon nanotubes for hydrogen storage, *J Nanosci Nanotechno*, 1 (2001) 7-29.
- [40] Y. Wang, Z.Q. Shi, Y. Huang, Y.F. Ma, C.Y. Wang, M.M. Chen, Y.S. Chen, Supercapacitor Devices Based on Graphene Materials, *J Phys Chem C*, 113 (2009) 13103-13107.
- [41] A.K. Geim, K.S. Novoselov, The rise of graphene, *Nat Mater*, 6 (2007) 183-191.
- [42] C.G. Liu, Z.N. Yu, D. Neff, A. Zhamu, B.Z. Jang, Graphene-Based Supercapacitor with an Ultrahigh Energy Density, *Nano Lett*, 10 (2010) 4863-4868.
- [43] Y. Wang, Y.P. Wu, Y. Huang, F. Zhang, X. Yang, Y.F. Ma, Y.S. Chen, Preventing Graphene Sheets from Restacking for High-Capacitance Performance, *J Phys Chem C*, 115 (2011) 23192-23197.
- [44] F.M. Hassan, V. Chabot, J.D. Li, B.K. Kim, L. Ricardez-Sandoval, A.P. Yu, Pyrrolic-structure enriched nitrogen doped graphene for highly efficient next generation supercapacitors, *J Mater Chem A*, 1 (2013) 2904-2912.
- [45] J.P. Zheng, T.R. Jow, A New Charge Storage Mechanism for Electrochemical Capacitors, *J Electrochem Soc*, 142 (1995) L6-L8.

[46] C. Lin, J.A. Ritter, B.N. Popov, Characterization of sol-gel-derived cobalt oxide xerogels as electrochemical capacitors, *J Electrochem Soc*, 145 (1998) 4097-4103.

[47] S.C. Pang, M.A. Anderson, T.W. Chapman, Novel electrode materials for thin-film ultracapacitors: Comparison of electrochemical properties of sol-gel-derived and electrodeposited manganese dioxide, *J Electrochem Soc*, 147 (2000) 444-450.

[48] K.C. Liu, M.A. Anderson, Porous nickel oxide/nickel films for electrochemical capacitors, *J Electrochem Soc*, 143 (1996) 124-130.

[49] R.N. Reddy, R.G. Reddy, Porous structured vanadium oxide electrode material for electrochemical capacitors, *J Power Sources*, 156 (2006) 700-704.

[50] C.C. Hu, W.C. Chen, K.H. Chang, How to achieve maximum utilization of hydrous ruthenium oxide for supercapacitors, *J Electrochem Soc*, 151 (2004) A281-A290.

[51] R.B. Rakhi, W. Chen, D.Y. Cha, H.N. Alshareef, Substrate Dependent Self-Organization of Mesoporous Cobalt Oxide Nanowires with Remarkable Pseudocapacitance, *Nano Lett*, 12 (2012) 2559-2567.

[52] S.F. Chin, S.C. Pang, M.A. Anderson, Self-assembled manganese dioxide nanowires as electrode materials for electrochemical capacitors, *Mater Lett*, 64 (2010) 2670-2672.

[53] J.W. Lee, T. Ahn, J.H. Kim, J.M. Ko, J.D. Kim, Nanosheets based mesoporous NiO microspherical structures via facile and template-free method for high performance supercapacitors, *Electrochim Acta*, 56 (2011) 4849-4857.

[54] B. Saravanakumar, K.K. Purushothaman, G. Muralidharan, Interconnected V₂O₅ Nanoporous Network for High-Performance Supercapacitors, *Acs Appl Mater Inter*, 4 (2012) 4484-4490.

[55] J. Li, I. Zhitomirsky, Electrophoretic deposition of manganese dioxide-carbon nanotube composites, *J Mater Process Tech*, 209 (2009) 3452-3459.

[56] A. Rudge, J. Davey, I. Raistrick, S. Gottesfeld, J.P. Ferraris, Conducting Polymers as Active Materials in Electrochemical Capacitors, *J Power Sources*, 47 (1994) 89-107.

[57] H.H. Zhou, H. Chen, S.L. Luo, G.W. Lu, W.Z. Wei, Y.F. Kuang, The effect of the polyaniline morphology on the performance of polyaniline supercapacitors, *J Solid State Electr*, 9 (2005) 574-580.

[58] H.L. Wang, Q.L. Hao, X.J. Yang, L.D. Lu, X. Wang, Graphene oxide doped polyaniline for supercapacitors, *Electrochem Commun*, 11 (2009) 1158-1161.

[59] J.J. Xu, K. Wang, S.Z. Zu, B.H. Han, Z.X. Wei, Hierarchical Nanocomposites of Polyaniline Nanowire Arrays on Graphene Oxide Sheets with Synergistic Effect for Energy Storage, *Acs Nano*, 4 (2010) 5019-5026.

[60] A. Davies, P. Audette, B. Farrow, F. Hassan, Z.W. Chen, J.Y. Choi, A.P. Yu, Graphene-Based Flexible Supercapacitors: Pulse-Electropolymerization of Polypyrrole on Free-Standing Graphene Films, *J Phys Chem C*, 115 (2011) 17612-17620.

[61] A. Burke, R&D considerations for the performance and application of electrochemical capacitors, *Electrochim Acta*, 53 (2007) 1083-1091.

[62] M.A. Pope, S. Korkut, C. Punckt, I.A. Aksay, Supercapacitor electrodes produced through evaporative consolidation of graphene oxide-water-ionic liquid gels, *J Electrochem Soc*, 160 (2013) A1653-A1660.

[63] V. Srinivasan, J.W. Weidner, Studies on the capacitance of nickel oxide films: Effect of heating temperature and electrolyte concentration, *J Electrochem Soc*, 147 (2000) 880-885.

[64] P. Azais, L. Duclaux, P. Florian, D. Massiot, M.A. Lillo-Rodenas, A. Linares-Solano, J.P. Peres, C. Jehoulet, F. Beguin, Causes of supercapacitors ageing in organic electrolyte, *J Power Sources*, 171 (2007) 1046-1053.

[65] M. Galinski, A. Lewandowski, I. Stepniak, Ionic liquids as electrolytes, *Electrochim Acta*, 51 (2006) 5567-5580.

[66] M.F. El-Kady, V. Strong, S. Dubin, R.B. Kaner, Laser Scribing of High-Performance and Flexible Graphene-Based Electrochemical Capacitors, *Science*, 335 (2012) 1326-1330.

[67] C.G. Cameron, Cold Temperature Optimization of Supercapacitors, *Ecs Transactions*, 41 (2012) 121-132.

[68] H.C. Wu, Y.P. Lin, E. Lee, W.T. Lin, J.K. Hu, H.C. Chen, N.L. Wu, High-performance carbon-based supercapacitors using Al current-collector with conformal carbon coating, *Mater Chem Phys*, 117 (2009) 294-300.

[69] B.L.Dutrow, C.M.Clark, X-ray Powder Diffraction (XRD), in, 2013.

[70] S. Swapp, Scanning Electron Microscopy (SEM), in, 2013.

[71] P. Analytical, Brunauer, Emmett, and Teller (BET) Theory, in, 2014.

[72] C.J. Gommès, Multi-layer adsorption: the BET adsorption isotherm, in, 2013.

[73] E.J.X. Pang, S.J. Pickering, A. Chan, K.H. Wong, P.L. Lau, N-type thermoelectric recycled carbon fibre sheet with electrochemically deposited Bi₂Te₃, *J Solid State Chem*, 193 (2012) 147-153.

[74] K.C. Tsay, L. Zhang, J.J. Zhang, Effects of electrode layer composition/thickness and electrolyte concentration on both specific capacitance and energy density of supercapacitor, *Electrochim Acta*, 60 (2012) 428-436.

[75] L.L. Zhang, T.X. Wei, W.J. Wang, X.S. Zhao, Manganese oxide-carbon composite as supercapacitor electrode materials, *Micropor Mesopor Mat*, 123 (2009) 260-267.

[76] S.H. Zhao, F. Wu, L.X. Yang, L.J. Gao, A.F. Burke, A measurement method for determination of dc internal resistance of batteries and supercapacitors, *Electrochem Commun*, 12 (2010) 242-245.

[77] R. Kotz, M. Carlen, Principles and applications of electrochemical capacitors, *Electrochim Acta*, 45 (2000) 2483-2498.

[78] W. Chen, R.B. Rakhi, L.B. Hu, X. Xie, Y. Cui, H.N. Alshareef, High-Performance Nanostructured Supercapacitors on a Sponge, *Nano Lett*, 11 (2011) 5165-5172.

[79] F.M. Hassan, V. Chabot, J. Li, B.K. Kim, L. Ricardez-Sandoval, A. Yu, Pyrrolic-structure enriched nitrogen doped graphene for highly efficient next generation supercapacitors, *Journal of Materials Chemistry A*, 1 (2013) 2904.

[80] J. Wang, Y.C. Song, Z.S. Li, Q. Liu, J.D. Zhou, X.Y. Jing, M.L. Zhang, Z.H. Jiang, In Situ Ni/Al Layered Double Hydroxide and Its Electrochemical Capacitance Performance, *Energy Fuel*, 24 (2010) 6463-6467.

[81] L.T. Lam, R. Louey, Development of ultra-battery for hybrid-electric vehicle applications, *J Power Sources*, 158 (2006) 1140-1148.

[82] A.S. Arico, P. Bruce, B. Scrosati, J.M. Tarascon, W. Van Schalkwijk, Nanostructured materials for advanced energy conversion and storage devices, *Nat Mater*, 4 (2005) 366-377.

[83] A.P. Yu, I. Roes, A. Davies, Z.W. Chen, Ultrathin, transparent, and flexible graphene films for supercapacitor application, *Appl Phys Lett*, 96 (2010).

[84] Z. You, K. Shen, Z.C. Wu, X.F. Wang, X.H. Kong, Electrodeposition of Zn-doped alpha-nickel hydroxide with flower-like nanostructure for supercapacitors, *Appl Surf Sci*, 258 (2012) 8117-8123.

[85] D.D. Zhao, S.J. Bao, W.H. Zhou, H.L. Li, Preparation of hexagonal nanoporous nickel hydroxide film and its application for electrochemical capacitor, *Electrochem Commun*, 9 (2007) 869-874.

[86] H.L. Wang, C.M.B. Holt, Z. Li, X.H. Tan, B.S. Amirkhiz, Z.W. Xu, B.C. Olsen, T. Stephenson, D. Mitlin, Graphene-nickel cobaltite nanocomposite asymmetrical supercapacitor with commercial level mass loading, *Nano Res*, 5 (2012) 605-617.

[87] B.E. Conway, V. Birss, J. Wojtowicz, The role and utilization of pseudocapacitance for energy storage by supercapacitors, *J Power Sources*, 66 (1997) 1-14.

[88] M. Jayalakshmi, K. Balasubramanian, Simple Capacitors to Supercapacitors - An Overview, *Int J Electrochem Sc*, 3 (2008) 1196-1217.

[89] Y.R. Ahn, M.Y. Song, S.M. Jo, C.R. Park, D.Y. Kim, Electrochemical capacitors based on electrodeposited ruthenium oxide on nanofibre substrates, *Nanotechnology*, 17 (2006) 2865-2869.

[90] A. Mirmohseni, M.S.S. Dorraji, M.G. Hosseini, Influence of metal oxide nanoparticles on pseudocapacitive behavior of wet-spun polyaniline-multiwall carbon nanotube fibers, *Electrochimica Acta*, 70 (2012) 182-192.

[91] J.M. Luo, B. Gao, X.G. Zhang, High capacitive performance of nanostructured Mn-Ni-Co oxide composites for supercapacitor, *Mater Res Bull*, 43 (2008) 1119-1125.

[92] A.A.F. Grupioni, E. Arashiro, T.A.F. Lassali, Voltammetric characterization of an iridium oxide-based system: the pseudocapacitive nature of the Ir_{0.3}Mn_{0.7}O₂ electrode, *Electrochimica Acta*, 48 (2002) 407-418.

[93] I.R.M. Kottegoda, N.H. Idris, L. Lu, J.Z. Wang, H.K. Liu, Synthesis and characterization of graphene-nickel oxide nanostructures for fast charge-discharge application, *Electrochimica Acta*, 56 (2011) 5815-5822.

[94] H.Y. Wu, H.W. Wang, Electrochemical Synthesis of Nickel Oxide Nanoparticulate Films on Nickel Foils for High-performance Electrode Materials of Supercapacitors, *Int J Electrochem Sc*, 7 (2012) 4405-4417.

[95] T. Xue, C.L. Xu, D.D. Zhao, X.H. Li, H.L. Li, Electrodeposition of mesoporous manganese dioxide supercapacitor electrodes through self-assembled triblock copolymer templates, *J Power Sources*, 164 (2007) 953-958.

[96] R.R. Jiang, T. Huang, J.L. Liu, J.H. Zhuang, A.S. Yu, A novel method to prepare nanostructured manganese dioxide and its electrochemical properties as a supercapacitor electrode, *Electrochimica Acta*, 54 (2009) 3047-3052.

[97] T. Zhu, J.S. Chen, X.W. Lou, Shape-controlled synthesis of porous Co₃O₄ nanostructures for application in supercapacitors, *Journal of Materials Chemistry*, 20 (2010) 7015-7020.

[98] S.L. Xiong, C.Z. Yuan, M.F. Zhang, B.J. Xi, Y.T. Qian, Controllable Synthesis of Mesoporous Co₃O₄ Nanostructures with Tunable Morphology for Application in Supercapacitors, *Chem-Eur J*, 15 (2009) 5320-5326.

[99] K.W. Nam, K.B. Kim, A study of the preparation of NiO_x electrode via electrochemical route for supercapacitor applications and their charge storage mechanism, *Journal of The Electrochemical Society*, 149 (2002) A346-A354.

[100] S.K. Meher, P. Justin, G.R. Rao, Pine-cone morphology and pseudocapacitive behavior of nanoporous nickel oxide, *Electrochimica Acta*, 55 (2010) 8388-8396.

- [101] P. Justin, S.K. Meher, G.R. Rao, Tuning of Capacitance Behavior of NiO Using Anionic, Cationic, and Nonionic Surfactants by Hydrothermal Synthesis, *J Phys Chem C*, 114 (2010) 5203-5210.
- [102] H. Jiang, T. Zhao, C.Z. Li, J. Ma, Hierarchical self-assembly of ultrathin nickel hydroxide nanoflakes for high-performance supercapacitors, *Journal of Materials Chemistry*, 21 (2011) 3818-3823.
- [103] E. Beach, S. Brown, K. Shqau, M. Mottern, Z. Warchol, P. Morris, Solvothermal synthesis of nanostructured NiO, ZnO and Co(3)O(4) microspheres, *Mater Lett*, 62 (2008) 1957-1960.
- [104] X. Sun, G. Wang, J.-Y. Hwang, J. Lian, Porous nickel oxide nano-sheets for high performance pseudocapacitance materials, *Journal of Materials Chemistry*, 21 (2011) 16581.
- [105] S.K. Meher, P. Justin, G.R. Rao, Microwave-mediated synthesis for improved morphology and pseudocapacitance performance of nickel oxide, *ACS applied materials & interfaces*, 3 (2011) 2063-2073.
- [106] J. Liu, S.F. Du, L.Q. Wei, H.D. Liu, Y.J. Tian, Y.F. Chen, Template-free synthesis of NiO hollow microspheres covered with nanoflakes, *Mater Lett*, 60 (2006) 3601-3604.
- [107] B.K. Kim, V. Chabot, A. Yu, Carbon nanomaterials supported Ni(OH)₂/NiO hybrid flower structure for supercapacitor, *Electrochim Acta*, 109 (2013) 370-380.

[108] C. Ge, Z. Hou, B. He, F. Zeng, J. Cao, Y. Liu, Y. Kuang, Three-dimensional flower-like nickel oxide supported on graphene sheets as electrode material for supercapacitors, *Journal of Sol-Gel Science and Technology*, 63 (2012) 146-152.

[109] M.-W. Xu, S.-J. Bao, H.-L. Li, Synthesis and characterization of mesoporous nickel oxide for electrochemical capacitor, *Journal of Solid State Electrochemistry*, 11 (2006) 372-377.

[110] E.E. Kalu, T.T. Nwoga, V. Srinivasan, J.W. Weidner, Cyclic voltammetric studies of the effects of time and temperature on the capacitance of electrochemically deposited nickel hydroxide, *J Power Sources*, 92 (2001) 163-167.

[111] J.W. Lang, L.B. Kong, W.J. Wu, Y.C. Luo, L. Kang, Facile approach to prepare loose-packed NiO nano-flakes materials for supercapacitors, *Chem Commun*, (2008) 4213-4215.

[112] C. Yuan, X. Zhang, L. Su, B. Gao, L. Shen, Facile synthesis and self-assembly of hierarchical porous NiO nano/micro spherical superstructures for high performance supercapacitors, *Journal of Materials Chemistry*, 19 (2009) 5772.

[113] W. Xing, F. Li, Z.-f. Yan, G.Q. Lu, Synthesis and electrochemical properties of mesoporous nickel oxide, *J Power Sources*, 134 (2004) 324-330.

[114] D.A. Corrigan, Effect of Coprecipitated Metal Ions on the Electrochemistry of Nickel Hydroxide Thin Films: Cyclic Voltammetry in 1M KOH, *Journal of The Electrochemical Society*, 136 (1989) 723.

[115] M.-S. Kim, A Study of the Electrochemical Redox Behavior of Electrochemically Precipitated Nickel Hydroxides Using Electrochemical Quartz Crystal Microbalance, Journal of The Electrochemical Society, 144 (1997) 1537.

[116] P.V. Kamath, Stabilized α -Ni(OH)₂ as Electrode Material for Alkaline Secondary Cells, Journal of The Electrochemical Society, 141 (1994) 2956.

[117] A.K. Shukla, S. Venugopalan, B. Hariprakash, Nickel-based rechargeable batteries, J Power Sources, 100 (2001) 125-148.

[118] H.L. Wang, H.S. Casalongue, Y.Y. Liang, H.J. Dai, Ni(OH)₂ Nanoplates Grown on Graphene as Advanced Electrochemical Pseudocapacitor Materials, J Am Chem Soc, 132 (2010) 7472-7477.

[119] C.-C. Hu, K.-H. Chang, T.-Y. Hsu, The Synergistic Influences of OH⁻ Concentration and Electrolyte Conductivity on the Redox Behavior of Ni(OH)₂/NiOOH, Journal of The Electrochemical Society, 155 (2008) F196.

[120] A. Di Fabio, A. Giorgi, M. Mastragostino, F. Soavi, Carbon-Poly(3-methylthiophene) Hybrid Supercapacitors, Journal of The Electrochemical Society, 148 (2001) A845.

[121] M.-S. Wu, H.-H. Hsieh, Nickel oxide/hydroxide nanoplatelets synthesized by chemical precipitation for electrochemical capacitors, Electrochimica Acta, 53 (2008) 3427-3435.

[122] J. Xu, X. Gu, J. Cao, W. Wang, Z. Chen, Nickel oxide/expanded graphite nanocomposite electrodes for supercapacitor application, *Journal of Solid State Electrochemistry*, 16 (2012) 2667-2674.

[123] H. Yang, G.H. Guai, C. Guo, Q. Song, S.P. Jiang, Y. Wang, W. Zhang, C.M. Li, NiO/Graphene Composite for Enhanced Charge Separation and Collection in p-Type Dye Sensitized Solar Cell, *The Journal of Physical Chemistry C*, 115 (2011) 12209-12215.

[124] M.-S. Wu, Y.-A. Huang, C.-H. Yang, Capacitive Behavior of Porous Nickel Oxide/Hydroxide Electrodes with Interconnected Nanoflakes Synthesized by Anodic Electrodeposition, *Journal of The Electrochemical Society*, 155 (2008) A798.

[125] W. Sugimoto, H. Iwata, K. Yokoshima, Y. Murakami, Y. Takasu, Proton and electron conductivity in hydrous ruthenium oxides evaluated by electrochemical impedance spectroscopy: The origin of large capacitance, *J Phys Chem B*, 109 (2005) 7330-7338.

[126] B. Seger, P.V. Kamat, Electrocatalytically Active Graphene-Platinum Nanocomposites. Role of 2-D Carbon Support in PEM Fuel Cells, *J Phys Chem C*, 113 (2009) 7990-7995.

[127] W.S. Hummers, R.E. Offeman, Preparation of Graphitic Oxide, *J Am Chem Soc*, 80 (1958) 1339-1339.

[128] C. Gomez-Navarro, R.T. Weitz, A.M. Bittner, M. Scolari, A. Mews, M. Burghard, K. Kern, Electronic transport properties of individual chemically reduced graphene oxide sheets, *Nano Lett*, 7 (2007) 3499-3503.

[129] V. Singh, D. Joung, L. Zhai, S. Das, S.I. Khondaker, S. Seal, Graphene based materials: Past, present and future, *Prog Mater Sci*, 56 (2011) 1178-1271.

[130] E. Bekyarova, M.E. Itkis, N. Cabrera, B. Zhao, A.P. Yu, J.B. Gao, R.C. Haddon, Electronic properties of single-walled carbon nanotube networks, *J Am Chem Soc*, 127 (2005) 5990-5995.

[131] Y.C. Si, E.T. Samulski, Exfoliated Graphene Separated by Platinum Nanoparticles, *Chem Mater*, 20 (2008) 6792-6797.

[132] A.P. Yu, H.W. Park, A. Davies, D.C. Higgins, Z.W. Chen, X.C. Xiao, Free-Standing Layer-By-Layer Hybrid Thin Film of Graphene-MnO₂ Nanotube as Anode for Lithium Ion Batteries, *J Phys Chem Lett*, 2 (2011) 1855-1860.

[133] J.S. Sakamoto, B. Dunn, Vanadium oxide-carbon nanotube composite electrodes for use in secondary lithium batteries, *Journal of The Electrochemical Society*, 149 (2002) A26-A30.

[134] C. Liu, F. Li, L.P. Ma, H.M. Cheng, Advanced Materials for Energy Storage, *Adv Mater*, 22 (2010) E28-+.

Appendix

I hereby declare that all images and tables reproduced in this thesis have been licensed for reuse. The standard Rightslink permission agreements can be provided upon request.

Content from my publications have been reproduced or altered with appropriate permissions if required [107].